



Fast high-precision distance metrology using a pair of modulator-generated dual-color frequency combs

C. WEIMANN,^{1,2,3,*} A. MESSNER,¹ T. BAUMGARTNER,¹ S. WOLF,¹
F. HOELLER,³ W. FREUDE,^{1,2} AND C. KOOS^{1,2,4}

¹*Institute of Photonics and Quantum Electronics (IPQ), Karlsruhe Institute of Technology (KIT) 76131 Karlsruhe, Germany*

²*Institute of Microstructure Technology (IMT), KIT 76344 Eggenstein-Leopoldshafen, Germany*

³*Corporate Research and Technology, Carl Zeiss AG, Oberkochen, Germany*

⁴*christian.koos@kit.edu*

**claudius.weimann@zeiss.com*

Abstract: We demonstrate fast high-precision non-contact distance measurements to technical surfaces using a pair of dual-color electro-optic frequency combs for synthetic-wavelength interferometry (SWI). The dual-color combs are generated from continuous-wave (cw) lasers at 1300 nm and 1550 nm, which are jointly fed to a pair of high-speed dual-drive Mach-Zehnder modulators. The dual-color approach is used for continuous and dead-zone-free compensation of temperature-induced fiber drift. We achieve standard deviations below 2 μm at an acquisition time of 9.1 μs for measurements through 7 m of single-mode fiber. Despite the technical simplicity of our scheme, our concept can well compete with other comb-based distance metrology approaches, and it can maintain its accuracy even under industrial operating conditions. The viability of the concept is demonstrated by attaching the fiber-coupled sensor head to an industrial coordinate measuring machine for acquisition of surface profiles of various technical samples. Exploiting real-time signal processing along with continuous fiber drift compensation, we demonstrate the acquisition of point clouds of up to 5 million data points during continuous movement of the sensor head.

© 2018 Optical Society of America under the terms of the [OSA Open Access Publishing Agreement](#)

1. Introduction

Optical distance metrology is at the heart of a wide variety of applications in science and industry, such as quality control, wear inspection, reverse engineering, forensics, and 3D scanning. Important requirements are high measurement precision, fast acquisition, and the ability to cope with natural technical surfaces characterized by roughness and strongly varying backscattered power levels. In the context of fast and precise distance metrology, optical frequency combs have emerged as valuable tools, either as light sources for the distance measurement itself [1–18], or as a means for calibrating lasers, e.g., for synthetic-wavelength interferometry (SWI) [19–21] or for frequency-modulated continuous wave (FMCW) laser ranging [22,23]. However, all these demonstrations rely on rather complex and sensitive setups that cannot cope with the stringent requirements that are associated with industrial applications. As an example, the majority of these demonstrations relies on free-space or fiber-based mode-locked lasers (MLL), which, despite considerable progress towards ruggedized implementations [24], are still characterized by considerable technical complexity, especially when it comes to operation in an uncontrolled industrial environment. Additional challenges arise in the context of dual-comb approaches, which generally require adjustment of both line spacing and center frequency along with stable operation without drift. Parametric comb generators [15] have that capability but rely on complex arrangements of phase modulators, injection-locked laser diodes, wavelength-division multiplexing splitters and combiners, high-power fiber amplifiers, as well as multiple nonlinear and linear fiber sections. Moreover, the majority of comb-

based distance metrology experiments are limited to laboratory demonstrations of the measurement system itself, using the fundamentally achievable precision as a benchmark. A system using dual frequency combs generated by electro-optic modulators has been demonstrated for measurements over baselines of up to 1.2 km [25]. However, only measurements to retro-reflectors are carried out with relatively long averaging times of 1 s for a single measurement, making the approach incompatible with the requirements associated with fast and dense digitization of technical surfaces. With a few exceptions [1,5], these demonstrations do not consider detrimental effects such as length drift of optical fibers and other thermal and mechanical influences that are unavoidable in real-world applications. It has been demonstrated that such effects can be compensated by using the partial end facet reflex of an optical fiber or a dedicated free-space reflector for a reference measurement [1,5], but this approach leads to dead spots in the measurement range when target and reference pulses overlap. Hence, despite the tremendous potential of many of the previously demonstrated comb-based distance measurement concepts, none of these approaches has demonstrated its applicability to industrial high-precision metrology.

In this paper, we demonstrate a robust, technically straightforward, and yet precise comb-based distance measurement concept that can maintain its precision even under realistic industrial boundary conditions. The concept relies on synthetic-wavelength interferometry (SWI) using a pair of dual-color frequency combs that are generated by a robust fiber-based system of commercially available off-the-shelf components such as continuous-wave (cw) lasers at 1300 nm and 1550 nm and standard telecom-grade dual-drive Mach-Zehnder modulators (MZM). The MZM are operated by fixed-frequency sinusoidal electrical signals, generating a pair of frequency combs for each wavelength. The pair of 1550 nm frequency combs is used for measuring the distance to the target, while the pair of 1300 nm combs is used solely for continuous dead-zone free detection and compensation of temperature-induced optical drift of the fiber that connects the comb measurement unit to a remote passive sensor head. To the best of our knowledge, our experiments represent the first demonstration of dead-zone-free drift compensation for comb-based distance measurements through optical fibers. The accuracy of the distance measurements relies on the line spacing of the respective frequency combs, which can be freely adjusted with high precision using electronic frequency references that are inherently traceable to widely available time standards. The ability to compensate fiber drift enables flexible installations of the passive sensor head on industrial kinematics such as a coordinate measuring machine (CMM) without impeding the measurement accuracy. In our experiments, we demonstrate standard deviations of 2 μm at an acquisition time of 9.1 μs for measurements through 7 m of standard single-mode fiber. Considering the accuracy in relation to the measurement time, our concept outperforms the majority of competing comb-based distance metrology demonstrations, despite its technical simplicity. Compared to time-of-flight based methods using sinusoidal intensity modulation or pulsed laser sources [3,26,27], where the accuracy is tightly linked to the bandwidth of the employed detection electronics, the chosen synthetic-wavelength approach decouples the achievable accuracy from the detector bandwidth. This allows using detection electronics with relatively moderate bandwidth under 2 GHz while achieving accuracy in the micrometer regime. For demonstrating operation under industrial conditions, we implement dedicated signal-processing algorithms on a field-programmable gate array (FPGA), achieving a real-time measurement rate of 3.3 kHz, which is only limited by the signal processing speed. The combination of continuous fiber-drift compensation and real-time signal processing allows for fast and dense digitization of three-dimensional surface profiles of technical samples featuring a wide range of rough naturally scattering surfaces. This is demonstrated by the acquisition of point clouds of up to 5 million data points, obtained from a sensor head that is continuously moved by an industrial coordinate measuring machine.

The paper is structured as follows: Section 2 provides details on the experimental setup and the comb-based distance measurement principle. Section 3 is dedicated to an in-depth characterization of the system performance and to a comparison with competing concepts. In

Section 4, we give a detailed description of our experimental demonstrations. The appendices A-F give mathematical details of the multi-heterodyne detection scheme and of the impact of noise on the measurement accuracy.

2. Experimental setup and measurement principle

2.1 Experimental setup of measurement system

A schematic of the measurement system is depicted in Fig. 1. The optical setup is entirely based on fiber-coupled, commercially available telecom-grade equipment. The light from two cw lasers with wavelengths of $\lambda_{\text{cal}} = 1300\text{nm}$ and $\lambda_{\text{obj}} = 1550\text{nm}$ and power levels of 15 dBm and 18 dBm respectively is split and combined by fiber couplers, feeding two Mach-Zehnder modulators (MZM1 and MZM2) for frequency comb generation. The light entering MZM2 is additionally frequency-shifted by a pair of acousto-optical modulators (AOM). The carrier at wavelength λ_{cal} is shifted by 80 MHz, the carrier at λ_{obj} by 55 MHz. The lithium-niobate MZM are driven by sinusoidal electrical signals with frequencies of 39.957 GHz for MZM1 and 40.000 GHz for MZM2. Both signal generators are referenced to a common clock signal (not depicted). The phase-modulated light shows broadband frequency comb spectra with line spacings that are precisely defined by the respective driving frequencies. By adjusting the bias voltage, the relative phase and the amplitudes of the driving signals between both arms of the modulator, spectrally flat frequency combs can be obtained [28,29].

The measured spectra are depicted in Fig. 1, Insets (1) and (2). The two frequency combs with a 39.957 GHz line spacing are referred to as signal combs, whereas the two frequency combs with a 40.000 GHz line spacing are named local oscillator (LO) combs. The superimposed signal combs are split by coupler CPL1 to propagate along a measurement path and along a reference path towards the optical receivers. In the same manner, the superimposed LO combs are split by coupler CPL2 and propagate towards the optical receivers. Each of the balanced receivers $R_{\text{x,meas}}$ and $R_{\text{x,ref}}$, which terminate the measurement paths and the reference paths, comprises a directional coupler followed by a pair of balanced photodiodes. Signal and LO combs are superimposed for heterodyne detection. Photomixing of the signal comb lines with their LO counterparts with detuned line spacing leads to a superposition of sinusoidal photocurrents at distinct intermediate frequencies (IF).

The polarization states of the signal combs are adjusted once at each start-up of the setup via polarization controllers in order to maximize the amplitude of the generated IF signals. Long-time polarization fluctuations, which could lead to polarization-induced fading of IF signal levels, are ignored in this proof-of-principle experiment and could in principle be compensated for by using a polarization diversity receiver structure [30]. The photocurrent spectrum is evaluated to find the relative distance to the surface of the measurement object and to simultaneously locate the position of the calibration mirror. The relative distances are calculated from the phase differences of the signals received by $R_{\text{x,meas}}$ with respect to the signals received at $R_{\text{x,ref}}$. Object and calibration information are discriminated by the respective carrier frequency shifts of 80 MHz and 55 MHz, which act as a label.

The signal combs are guided to a sensor head mounted on a coordinate measuring machine (CMM) via 7 m of standard single-mode fiber. In the sensor head, the signal combs exit the fiber and are separated by a dichroic beam splitter cube (BS) upon collimation of the beam. The BS is transparent for the frequency comb around the center wavelength λ_{cal} . This comb then propagates to a fixed calibration mirror, is reflected and coupled back via the fiber and coupler CPL3 to the receiver $R_{\text{x,meas}}$.

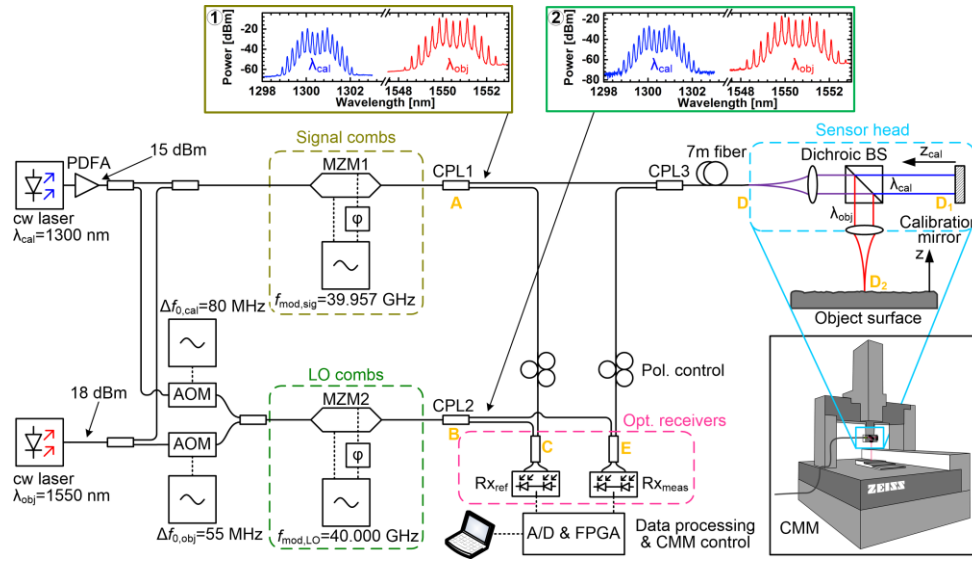


Fig. 1. Experimental setup. Light from two continuous wave (cw) lasers with wavelengths of $\lambda_{\text{cal}} = 1300$ nm and $\lambda_{\text{obj}} = 1550$ nm and power levels of 15 dBm and 18 dBm, respectively, is split and fed to two Mach-Zehnder modulators (MZM1, MZM2). Light guided to MZM2 is additionally frequency-shifted by 80 MHz and 55 MHz, respectively, using acousto-optic modulators (AOM). The MZM are driven with strong sinusoidal signals (peak voltage 6.3 V) at frequencies of 39.957 GHz and 40.000 GHz, respectively. Proper adjustment of phase and amplitude of the driving signal in one arm of a MZM leads to broadband frequency comb generation. In the following, optical paths are described in terms of the points A ... E depicted in the setup sketch (bold, orange letters). The signal combs (Inset 1) are split in fiber coupler CPL1. One part is incident on the balanced photodetector (BD) Rx_{ref} after propagation over the internal optical path AC. The other part is guided through CPL3 to a sensor head via path AD. A dichroic beam splitter (BS) in the sensor head separates λ_{cal} and λ_{obj} . The calibration comb centered at λ_{cal} is reflected from a fixed calibration mirror, the object comb centered at λ_{obj} is scattered back from the object surface. The reflected light is coupled back into the fiber and guided to Rx_{meas} via path ADD₁DE and ADD₂DE, respectively. On both receivers, the signal combs are superimposed with the frequency-shifted local oscillator (LO) combs featuring detuned line spacing (Inset 2) for heterodyne detection. Polarization controllers (Pol. control) are adjusted once at each start-up of the setup. The generated photocurrents are acquired by an analog-to-digital (A/D) converter, and a Fourier transformation is used to isolate the discrete beat notes of the signal and LO combs lines. Digital signal processing is implemented on a field-programmable gate array (FPGA) and a personal computer. The optical path lengths D_2D and D_1D are denoted as z (object height) and z_{cal} . PDFA: Praseodymium-doped fiber amplifier. CMM: Coordinate measuring machine.

The frequency comb with center wavelength λ_{obj} is reflected by the BS and focused onto the object surface by a lens with a focal length of 30 mm and a diameter larger than the diameter 3.4 mm of the collimated beam. The resulting numerical aperture amounts to 0.057. Assuming a Gaussian beam, the beam illuminating the object surface exhibits a beam waist diameter of 17.4 μm , which defines the lateral resolution. The scattered light collected by the lens is coupled back into the fiber and guided to the receiver Rx_{meas} as well.

The applied heterodyne reception technique enables sensitive detection of signals with low power [31]. The IF signals are analog-to-digital converted with 1.8 GSa/s and 12 bit resolution, and a discrete Fourier transform (DFT) is performed. The DFT operates on $2^{14} = 16384$ samples and is implemented on a field-programmable gate array (FPGA). The DFT results are then fed to a personal computer (PC) for further processing.

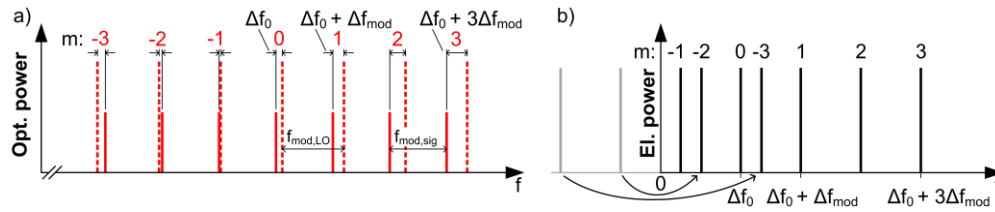


Fig. 2. Detection principle. (a) Schematic optical spectra of signal comb (continuous lines) and LO comb (dashed lines). The line spacings of signal and LO comb are slightly detuned by $\Delta f_{\text{mod}} = |f_{\text{mod,LO}} - f_{\text{mod,sig}}|$, and the center frequencies are offset by Δf_0 . (b) Schematic one-sided power spectrum of the photocurrent. Quadratic detection of signal and LO comb by a photodiode leads to a multitude of sinusoidal IF signals with frequencies $|\Delta f_0 + m\Delta f_{\text{mod}}|$ in the photocurrent. Negative frequencies of the corresponding two-sided spectrum are drawn in gray and mirrored to positive frequencies of the one-sided spectrum. The phases of the IF signals are directly linked to the phase shifts accumulated by the lines of the FC during propagation.

While the recording of the samples takes only 9.1 μs , the complete real-time measurement rate is currently limited to 3.3 kHz by the processing time required for the DFT. As presently only two Fourier transforms are calculated in parallel, future implementations could realize higher real-time measurement rates by a deeper parallelization. The chosen acquisition time and associated DFT length represents a trade-off between measurement rate and precision and allows us to achieve micrometer precision while still maintaining the ability for fast and dense sample digitization. The PC controls the CMM via Ethernet and reads the position of the sensor head with reference to the coordinate system of the CMM. By moving the sensor head across the object surface while optically measuring the height z , surface profiles can be recorded. The CMM is also used for tactile height measurements, which serve as “true” reference data for comparison with the optically obtained results.

2.2 Measurement principle and data processing

The measurement principle is based on synthetic wavelength interferometry, evaluating the phase difference of the propagators $\exp(-j\omega_{l,\text{sig}} 2z/c)$ of the reflected signal comb lines l with (angular) frequency $\omega_{l,\text{sig}} = 2\pi f_{l,\text{sig}}$ and c as the vacuum speed of light [1,11,32]. Using two signal combs with different center wavelengths λ_{cal} and λ_{obj} and a calibration mirror in a fixed calibration distance z_{calib} , two independent distance measurements are made simultaneously for compensating the temperature drift of the fibers.

The measurement principle is first explained for only one set of signal comb and LO comb. The signal comb lines are numbered by the integer l and have discrete optical frequencies $f_{l,\text{sig}} = f_{0,\text{sig}} + lf_{\text{mod,sig}}$, where $f_{0,\text{sig}} = c/\lambda_{0,\text{sig}}$ is defined by the input cw laser, and where $f_{\text{mod,sig}}$ is the driving frequency for the MZM. The LO comb’s center frequency is shifted with an AOM by Δf_0 , and its line spacing is detuned by the difference in MZM driving frequencies Δf_{mod} . The integer m denotes the order of the LO comb lines with optical frequencies $f_{m,\text{LO}} = f_{0,\text{LO}} + mf_{\text{mod,LO}} = (f_{0,\text{sig}} + \Delta f_0) + m(f_{\text{mod,sig}} + \Delta f_{\text{mod}})$. The comb lines of signal comb and LO comb are superimposed on the receivers Rx in Fig. 1. The superposition of signal and LO comb spectra is illustrated in Fig. 2(a) with 7 comb lines for each comb, $l, m = -3, \dots, 0, \dots, 3$. Quadratic detection leads to a multitude of sinusoidal photocurrents at distinct intermediate frequencies (IF) in the baseband. With an integer m denoting the order of the comb lines, the photocurrent shows N spectral lines at frequencies $|\Delta f_0 + m\Delta f_{\text{mod}}|$, as depicted schematically in Fig. 2(b). A rigorous mathematical description of the measurement scheme can be found in Appendix A.

In the following, optical paths are described in terms of the points A ... E depicted in the setup sketch of Fig. 1. The optical path lengths are denoted as z for path D_2D , $D_{\text{sig,meas}}$ for path ADE, $D_{\text{LO,meas}}$ for path BE, $D_{\text{sig,ref}}$ for path AC, and $D_{\text{LO,ref}}$ for path BC. The phases

$\varphi_m(2z + D_{\text{sig,meas}}, D_{\text{LO,meas}})$ of the IF signal received by Rx_{meas} for variable object positions z are compared to the reference phases $\varphi_m(D_{\text{sig,ref}}, D_{\text{LO,ref}})$ of IF signal received by Rx_{ref} . The optical path length difference between the measurement and the reference path can be extracted from the phase differences $\Delta\varphi_m(z) = \varphi_m(2z + D_{\text{sig,meas}}, D_{\text{LO,meas}}) - \varphi_m(D_{\text{sig,ref}}, D_{\text{LO,ref}})$, see Appendix A, Eq. (36).

The optical path lengths $D_{\text{sig,meas}}(t), D_{\text{sig,ref}}(t), D_{\text{LO,meas}}(t)$ and $D_{\text{LO,ref}}(t)$ inside fibers are subject to variations as a function of time t due to temperature changes [33–35]. The quantities $L_{\text{sig,meas}}(t), L_{\text{sig,ref}}(t), L_{\text{LO,meas}}(t)$ and $L_{\text{LO,ref}}(t)$ denote the actual geometric path lengths for the signal comb and the LO comb at a given time t . Note that these path lengths already consider the fact that the light may propagate back and forth through the same physical section of a path. In detail, $L_{\text{sig,meas}}, L_{\text{LO,meas}}, L_{\text{sig,ref}}, L_{\text{LO,ref}}$ represent the geometrical lengths of paths ADE, BE, AC, and BC, respectively. We further denote n as the group refractive index, dn/dT as the thermo-optic coefficient, $\alpha_L = (dL/dT)/L$ as the thermal expansion coefficient. Moreover, we use the length-averaged temporal temperature differences with respect to a reference time t_0 of the various fiber paths. For path ADE (length $L_{\text{sig,meas}}$), these temperature differences are denoted as $\Delta T_{\text{sig,meas}} = T_{\text{sig,meas}}(t) - T_{\text{sig,meas}}(t_0)$, and the temperature differences for the other paths are obtained by replacing the subscript ‘sig’ by ‘LO’ and/or ‘meas’ by ‘ref’. The optical path length $D_{\text{sig,meas}} = nL_{\text{sig,meas}}$ varies with temperature according to $dD_{\text{sig,meas}} = (nd(L_{\text{sig,meas}})/dT + L_{\text{sig,meas}} d(n)/dT)dT$. Using the previous definitions, this leads to temporal optical path length variations

$$\Delta D_{\text{sig,meas}}(t) = \left(n\alpha_L + \frac{dn}{dT} \right) L_{\text{sig,meas}} \Delta T_{\text{sig,meas}}(t). \quad (1)$$

The temporal optical path length variations for the other paths are obtained by replacing the subscript ‘sig’ by ‘LO’ and/or ‘meas’ by ‘ref’. The considerably smaller temperature-dependent path length changes of the free-space segment z can be neglected. As a consequence, the phase differences between measurement and reference path $\Delta\varphi_m(z, t)$ now depend also on time,

$$\Delta\varphi_m(z, t) = \frac{m\omega_{\text{mod,sig}}}{c} \left[2z + D_{\text{sig,meas}}(t) - D_{\text{LO,meas}}(t) - (D_{\text{sig,ref}}(t) - D_{\text{LO,ref}}(t)) \right] + g(z, t) - (D_{\text{LO,meas}}(t) - D_{\text{LO,ref}}(t))m\Delta\omega_{\text{mod}}/c \quad (2)$$

The function $g(z, t)$ depends on time, but not on m ,

$$g(z, t) = (2z + D_{\text{sig,meas}}(t) - D_{\text{LO,meas}}(t) - (D_{\text{sig,ref}}(t) - D_{\text{LO,ref}}(t)))\omega_{0,\text{sig}}/c - (D_{\text{LO,meas}}(t) - D_{\text{LO,ref}}(t))\Delta\omega_0/c, \quad (3)$$

see Appendix A, Eq. (36). The object height z is extracted by fitting a straight line to the 2π -unwrapped data points $\Delta\varphi_m(z, t)$ and by evaluating its slope with respect to a zero measurement at $z_0 = 0, t_0 = 0$, see Appendix A, Eq. (38),

$$\frac{d\Delta\varphi_m(z, t)}{dm} \Big|_{z_0=0, t_0=0} = \frac{\omega_{\text{mod,sig}}}{c} \left(2z + \Delta D_{\text{sig,meas}}(t) - \Delta D_{\text{LO,meas}}(t) - (\Delta D_{\text{sig,ref}}(t) - \Delta D_{\text{LO,ref}}(t)) \right) \quad (4)$$

Obviously, the thermally induced variations of optical path lengths $\Delta D_{\text{sig,meas}}(t), \Delta D_{\text{LO,meas}}(t), \Delta D_{\text{sig,ref}}(t)$ and $\Delta D_{\text{LO,ref}}(t)$ lead to an error when extracting the distance z from the slope of the phases as a function of comb line index m . We estimate the magnitude of this error by using

published data. In a single-mode fiber with $n = 1.4679$ [36], $\alpha_L \approx 0.5 \times 10^{-6} \text{ K}^{-1}$ [34,37,38], $dn/dT \approx 10 \times 10^{-6} \text{ K}^{-1}$ [33,34,37–39], the temperature-induced relative optical path length change can be quantified as (dropping the subscripts)

$$(\Delta D/\Delta T)/L = 10.7 \mu\text{m}/(\text{K m}). \quad (5)$$

In practically relevant systems, typical fiber lengths are in the meter range (say, 10 m) and temperature changes of a few Kelvin (say, 10 K) are to be expected in a normal industrial environment. As a consequence, accuracies better than 1 mm require a calibration technique, which allows to independently determine the temperature-induced variations of the various fiber paths. To this end, we perform a second measurement with frequency combs at a different center wavelength $\lambda_{\text{cal}} = 1300 \text{ nm}$ using a fixed calibration mirror at position D_1 , Fig. 1. The 1300 nm-combs along with the previous combs at $\lambda_{\text{obj}} = 1550 \text{ nm}$ are generated from two cw lasers by identical modulators, propagate through the same fiber and are separated only in the sensor head by the dichroic beam splitter. Calibration and object measurements are separately evaluated by heterodyne down-conversion to different intermediate frequencies – a measurement of a typical electrical power spectrum of the photocurrent is depicted in Fig. 3(a). The IF signals for λ_{obj} and λ_{cal} are centered around different offset frequencies $\Delta f_{0,\text{obj}}$ and $\Delta f_{0,\text{cal}}$ as defined by the two AOM. The associated lines can hence be extracted from the photocurrent spectrum, and the associated optical path lengths can be evaluated separately. In the following, the optical calibration path length is denoted as z_{cal} , which refers to path D_1D , see Fig. 1. We apply Eq. (4) for the object and the calibration comb, introduce the effective optical path lengths $D_{\text{obj}}(t)$ and $D_{\text{cal}}(t)$ for the object wavelength λ_{obj} and the calibration wavelength λ_{cal} , with corresponding refractive indices $n_{\lambda_{\text{obj}}}$ and $n_{\lambda_{\text{cal}}}$, and find for the difference

$$\frac{d(\Delta\varphi_{m,\text{obj}}(z,t))}{dm} - \frac{d(\Delta\varphi_{m,\text{cal}}(z,t))}{dm} = \frac{\omega_{\text{mod,sig}}}{c} [2(z - z_{\text{cal}}) + D_{\text{obj}}(t) - D_{\text{cal}}(t)],$$

$$D_{\text{obj}}(t) = n_{\lambda_{\text{obj}}}(t)L_{\text{sig,meas}}(t) - n_{\lambda_{\text{obj}}}(t)L_{\text{LO,meas}}(t) - n_{\lambda_{\text{obj}}}(t)L_{\text{sig,ref}}(t) + n_{\lambda_{\text{obj}}}(t)L_{\text{LO,ref}}(t),$$

$$D_{\text{cal}}(t) = n_{\lambda_{\text{cal}}}(t)L_{\text{sig,meas}}(t) - n_{\lambda_{\text{cal}}}(t)L_{\text{LO,meas}}(t) - n_{\lambda_{\text{cal}}}(t)L_{\text{sig,ref}}(t) + n_{\lambda_{\text{cal}}}(t)L_{\text{LO,ref}}(t).$$

If the group refractive index and the thermo-optic coefficient for the measurement and the calibration combs were identical, we had $D_{\text{obj}}(t) = D_{\text{cal}}(t)$, and the temperature fluctuations would compensate exactly, see Eq. (1). However, there is an actual wavelength dependency of n and dn/dT [34,36], and this leads to a remaining differential temperature drift of the individual optical path lengths of (dropping again all individual subscripts)

$$((\Delta D_{\text{obj}}/\Delta T) - (\Delta D_{\text{cal}}/\Delta T))/L = 32 \text{ nm}/(\text{K m}). \quad (7)$$

Comparing this result to Eq. (5), we find that the calibration measurement reduces the temperature influence by three orders of magnitude.

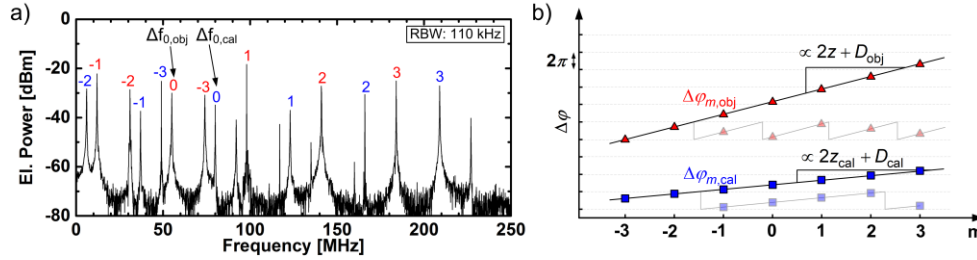


Fig. 3. Detection principle and data processing. (a) Measured one-sided spectrum of the photocurrent in a resolution bandwidth (RBW) of 110 kHz. The spectral lines of the photocurrent are indexed by m as in Fig. 2. For the object comb (red) $m = 0$ refers to the spectral line at the offset frequency $\Delta f_{0,\text{obj}} = 55$ MHz, and for the calibration comb (blue) to the line at offset frequency $\Delta f_{0,\text{cal}} = 80$ MHz. The appearance of negative frequencies ($m < -1$ in the present configuration) in the one-sided electrical spectrum is explained in Fig. 2. (b) Differences of the IF phases $\Delta\varphi_{m,\text{obj}}$ and $\Delta\varphi_{m,\text{cal}}$ as measured between the reference and the measurement receiver for object and calibration comb as a function of the line index m . Phase values before unwrapping (saw-tooth-like shapes) are depicted in light colors, illustrating the 2π -periodicity. The unwrapped phase values follow a linear relationship. The slopes of the fitted straight lines are proportional to the respective optical length differences between reference and measurement paths. Triangles mark the phase slopes according to Eq. (4), where $D_{\text{obj}}(t)$ and $D_{\text{cal}}(t)$ are defined in Eq. (6).

The slopes $d(\Delta\varphi_{m,\text{obj}}(z,t))/dm$ and $d(\Delta\varphi_{m,\text{cal}}(z,t))/dm$ used in Eq. (6) are determined by a linear regression, as illustrated in Fig. 3(b). Note that the measurement does only permit to determine the phase values up to an integer multiple of 2π , and that the measured phases have to be unwrapped before extracting the slope. This determines the unambiguity range Δz_{ua} of the approach: In Eq. (4), the quantities D can be assumed to be constant. The maximum change $\Delta(\Delta\varphi_m(z,t))$ which can be uniquely measured is 2π . The associated maximum unambiguously detectable change of Δz_{ua} hence corresponds to a phase shift of 2π between neighboring comb lines ($\Delta m = 1$) and can be expressed as

$$\Delta z_{\text{ua}} = \frac{2\pi c}{2\omega_{\text{mod,sig}}} = \frac{1}{2} \Lambda_1, \quad \Lambda_m = \frac{c}{m f_{\text{mod,sig}}}. \quad (8)$$

The quantity Λ_1 corresponds to the biggest synthetic wavelength [40] used in the measurement, see Appendix A Eq. (34). For our system we have $f_{\text{mod,sig}} = 39.957$ GHz, leading to an unambiguity range of $\Delta z_{\text{ua}} = c/(2f_{\text{mod,sig}}) = 3.7$ mm. This range could be extended by, e. g., subsequent measurements with different comb line spacings $f_{\text{mod,sig}}$ [1,12], by a combination with longer-range time-of-flight measurement schemes [21], or by using special schemes in which the LO comb also propagates to the measurement target [41].

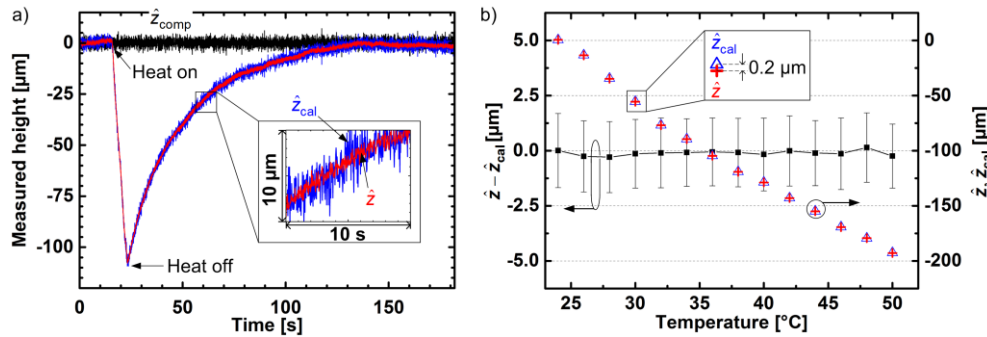


Fig. 4. Influence of fiber temperature drift on the measured object height, and compensation of this drift. (a) Qualitative demonstration. A section of fiber CPL3-D in Fig. 1 is rapidly heated for a few seconds with a heat gun. The measured object height \hat{z} decreases during the heating period due to expansion of the fiber and approaches its true value $z = 0$ while cooling down (solid red, $\lambda = 1550$ nm). The measured calibration height \hat{z}_{cal} follows this curve closely (solid blue, $\lambda = 1300$ nm), but exhibits more noise because of the lower optical comb power, see inset. The difference $\hat{z}_{\text{comp}} = \hat{z} - \hat{z}_{\text{cal}}$, which measures the true temperature-compensated object height (black) z with reference to z_{cal} , remains unaffected. (b) Quantitative demonstration. A 0.5 m-long section of the optical fiber path CPL3-D is immersed in a water bath which is heated in 2 K steps. At each temperature step, the distances \hat{z} and \hat{z}_{cal} to fixed targets at z and z_{cal} , respectively, are measured 500 times. Blue triangles and red crosses denote the measured averages $\langle \hat{z} \rangle$ and $\langle \hat{z}_{\text{cal}} \rangle$, respectively (vertical axis on the right). The black squares represent the averages of the differences $\langle \hat{z}_{\text{comp}} \rangle$ (vertical axis left), and the error bars indicate ± 1 standard deviation $\sigma_{\hat{z}_{\text{comp}}}$. The optical fields traverse the heated fiber section twice so that the relevant geometrical path length is $L_h = 2 \times 0.5$ m. While the true height z remains constant, the measured object and calibration heights \hat{z} and \hat{z}_{cal} change because the optical path length D_h of the heated fiber section for 1550 nm and 1300 nm changes with a linear coefficient of $(2\Delta\hat{z}/\Delta T)/L_h = (\Delta D_h/\Delta T)/L_h = (14.8 \pm 0.5) \mu\text{m}/(\text{K m})$ according to Eq. (4), (5), while \hat{z}_{comp} remains constant.

3. System characterization

In the following we demonstrate the efficiency of our path-length-drift compensation scheme when the system is exposed to deterministic and stochastic changes of the ambient temperature. If environmental changes are compensated, the limiting measurement accuracy is determined by the system's signal-to-noise power ratio.

3.1 Deterministic time-dependent system uncertainties due to thermal path length changes

The experimental results can be seen in Fig. 4(a) for a qualitative demonstration. A 5 m long fiber leading to the sensor head is heated for a few seconds with a heat gun, while continuously measuring the distance to a fixed spot on an static object. The individual measurement results for the true heights z and z_{cal} are named $\hat{z} = z + 0.5D_{\text{obj}}(t)$ and $\hat{z}_{\text{cal}} = z + 0.5D_{\text{cal}}(t)$ and are displayed as red and blue curves in Fig. 4(a). These measurement data exhibit a strong temperature drift – the optical path length expands during the heating phase, and shrinks again while the fiber is cooling down. However, the difference,

$$\hat{z}_{\text{comp}} = \hat{z} - \hat{z}_{\text{cal}}, \quad (9)$$

(black curve) stays constant, Fig. 4(a). A quantitative characterization was done by a controlled heating of a 0.5 m-long section of the fiber in a water bath, Fig. 4(b). No heatsinks were applied outside this 0.5 m-range.

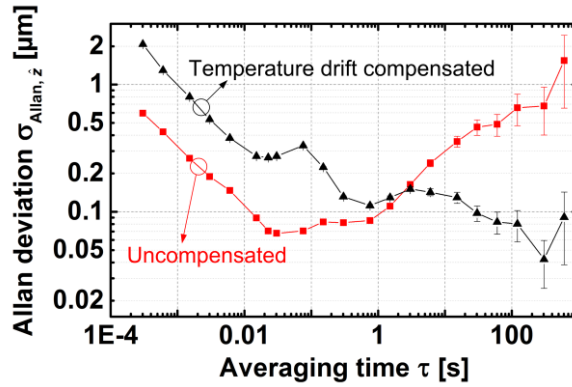


Fig. 5. Allan deviations calculated from repeated measurements to a mirror at a fixed distance. Result for uncompensated measurements shown in red, result for temperature-drift-compensated measurements shown in black.

Each temperature step was followed by sufficient settling time of around half an hour. Increasing the temperature while measuring a constant object height results in a relative optical path length change $(\Delta D/\Delta T)/L = (14.8 \pm 0.5) \mu\text{m}/(\text{K m})$. This is in fair agreement with the value of $10.7 \mu\text{m}/(\text{K m})$ that was estimated from published data of other groups, Eq. (5). The discrepancy is attributed to heat conduction along the fiber, which increases the effective heated length. The temperature-compensated height $\hat{z}_{\text{comp}} = \hat{z} - \hat{z}_{\text{cal}}$ stays constant within the measurement accuracy over the whole temperature range, demonstrating the effectiveness of the compensation scheme.

3.2 Stochastic time-dependent system uncertainties due to path length fluctuations

During extended measurement times, the optical path length varies due to random refractive index fluctuations of the air in the free-space path, and because of the remaining uncompensated optical fiber path length fluctuation due to the wavelength dependency of n and dn/dT , see Eq. (7) and associated text. For quantifying the stability of the system, we record a number of values \hat{z} at time intervals Δt and subdivide the total measurement time into subperiods of duration $\tau = N\Delta t$, which are subscripted by n . Each subperiod n therefore comprises $\nu = 1, 2, \dots, N$ data points $\hat{z}_{n,\nu}$. As a measure for the long-term stability we use the Allan variance:

$$\sigma_{\text{Allan},\hat{z}}^2(\tau) = \frac{1}{2} \left\langle \left(\langle \hat{z}_{n+1} \rangle_{\tau} - \langle \hat{z}_n \rangle_{\tau} \right)^2 \right\rangle_n, \quad \langle \hat{z}_n \rangle_{\tau} = \frac{1}{N} \sum_{\nu=1}^N \hat{z}_{n,\nu}, \quad \tau = N\Delta t, \quad (10)$$

where the brackets $\langle \rangle$ denote the average of the respective quantity. For repeated uncompensated measurements $\hat{z}_{n,\nu}$ under nominally stable environmental conditions, the resulting Allan deviation $\sigma_{\text{Allan},\hat{z}}$ is plotted in Fig. 5. For short averaging times τ , random fluctuations lead to a relatively large $\sigma_{\text{Allan},\hat{z}}$, which decreases as the averaging time τ increases. However, the averaging does not help for long-term drifts, e.g., on a time scale of 1s or more, where the Allan deviation of the uncompensated measurements starts increasing again.

This can be overcome by the dual-wavelength drift compensation scheme. In a second experiment, we record the Allan deviation for the compensated measurement value $\hat{z}_{\text{comp}} = \hat{z} - \hat{z}_{\text{cal}}$ as defined in Eq. (9). Note that, for small averaging times, the resulting Allan deviation $\sigma_{\text{Allan},\hat{z}_{\text{comp}}}$ of the compensated measurements is larger than the Allan deviations $\sigma_{\text{Allan},\hat{z}}$ of the uncompensated scheme. This is caused by smaller comb power and hence the higher noise levels of the calibration measurement in combination with the fact that the variance of a sum of the two independent random variables $\langle \hat{z}_n \rangle_{\tau}$ and $\langle \hat{z}_{\text{cal},n} \rangle_{\tau}$ equals the sum of the variances $\sigma_{\langle \hat{z} \rangle}^2 + \sigma_{\langle \hat{z}_{\text{cal}} \rangle}^2$. For long averaging times or for measurements over extended periods, long-term

drifts dominate the Allan deviation of the uncompensated measurements, while the compensated measurement reduces the effect of such drifts significantly.

Our current real-time measurement rate is $1/\Delta t = 3.3\text{kHz}$. For typical surface scans as conducted in our proof-of-principle demonstrations, we record around 10^6 data points which takes around 300s. The Allan deviation of the compensated measurement (black curve, Fig. 5) is as small as 60 nm. Without compensation (red curve, Fig. 5), the additional measurement uncertainty would be much larger, even in the case of a nominally stable laboratory environment. To achieve high precision with a fiber-based system in an uncontrolled workshop environment, temperature drift compensation is indispensable.

3.3 Measurement precision dependent on signal-to-noise power ratio

When temperature-related measurement errors are compensated, the measurement precision of the system is eventually limited by noise. We therefore quantify the influence of various sources of noise: Phase noise and relative intensity noise (RIN) of the comb sources, shot noise (quantum noise) in the photodiode current, noise of the transimpedance amplifiers (TIA) that amplify the photocurrent, quantization noise of the analog-to-digital converter, and stochastic crosstalk from the finite isolation of the 3 dB splitter (CPL3 in Fig. 1).

It turns out that for the operating conditions of interest, quantization noise is negligible. Moreover, because we employ a self-heterodyne detection scheme, phase noise of the source is not transferred to the photodetector current. The influence of the remaining noise sources on the signal-to-noise power ratio (SNR) and on the overall distance measurement accuracy is discussed in the following paragraphs.

Relative intensity noise: Although mitigated by the balanced detection scheme, relative intensity noise (RIN) of the optical carriers still leads to some fluctuation of the photocurrent amplitude and the associated voltage signal. The corresponding relations are derived in Appendix B and C. The quantity S_λ (unit A/W) is the detector sensitivity, R_{TIA} (unit Ω) denotes the transimpedance gain of the TIA unit, $\text{RIN}_{\text{spec},\lambda}$ is the height of the RIN spectral density of the respective laser with center wavelength λ , and Δf is the detection bandwidth. Assuming total optical comb powers $P_{\text{sig},\lambda}$ and $P_{\text{LO},\lambda}$, respectively, the resulting noise variance of the voltage is given as [42]

$$\sigma_{\text{RIN}}^2 = \sum_{\lambda} (S_\lambda R_{\text{TIA}})^2 \text{RIN}_{\text{spec},\lambda} P_{\text{LO},\lambda} P_{\text{sig},\lambda} \Delta f, \quad (11)$$

where the sum \sum_{λ} comprises the two wavelengths $\lambda_{\text{obj}} = 1550\text{nm}$ and $\lambda_{\text{cal}} = 1300\text{nm}$.

Shot noise: The shot noise (quantum noise) variance of the voltage (unit V^2) at the output of the balanced photodetectors (BD) in the receivers Rx_{meas} and Rx_{ref} depends on the total optical comb power $P_{\text{sig},\lambda} + P_{\text{LO},\lambda}$ impinging on the detector for each center wavelength $\lambda = \{\lambda_{\text{obj}}, \lambda_{\text{cal}}\}$:

$$\sigma_{\text{shot}}^2 = 2e \sum_{\lambda} S_\lambda (P_{\text{sig},\lambda} + P_{\text{LO},\lambda}) R_{\text{TIA}}^2 \Delta f. \quad (12)$$

Noise-equivalent power: Noise of a photodetector system is usually specified in terms of its noise-equivalent power (NEP), which includes the effects of photodetector quantum noise and electronic noise of the TIA. The resulting noise variance of the voltage is:

$$\sigma_{\text{TIA}}^2 = (R_{\text{TIA}} \text{NEP} \cdot S_{\text{NEP}})^2 \Delta f. \quad (13)$$

The quantity S_{NEP} stands for the photodetector sensitivity at the wavelength where the NEP was measured by the manufacturer of the device. In Appendix D, we show that σ_{TIA}^2 is dominated by electronic noise contributions.

These noise contributions lead to a finite signal-to-noise ratio (SNR). According to Eq. (32) in Appendix A, the signal amplitude $\hat{V}_{m,\lambda}$ of a sinusoidal voltage generated by heterodyne mixing of the m -th lines of signal comb and LO comb (see Fig. 2) is given by:

$$\hat{V}_{m,\lambda} = S_{\lambda} \sqrt{2P_{m,\text{sig},\lambda} 2P_{m,\text{LO},\lambda}} R_{\text{TIA}}, \quad (14)$$

where $P_{m,\text{sig},\lambda}$ and $P_{m,\text{LO},\lambda}$ denote the comb line powers of the signal and the LO comb.

Relative intensity noise of the source, photodetector shot noise, and TIA noise are independent so that their variances can be added for a total noise variance $\sigma_{\text{tot}}^2 = \sigma_{\text{RIN}}^2 + \sigma_{\text{Shot}}^2 + \sigma_{\text{TIA}}^2$. The SNR for the m -th IF line from combs with a center wavelength λ is then:

$$\text{SNR}_{m,\lambda} = \frac{\frac{1}{2} \hat{V}_{m,\lambda}^2}{\sigma_{\text{tot}}^2} = \frac{\frac{1}{2} S_{\lambda}^2 R_{\text{TIA}}^2 2P_{m,\text{sig},\lambda} 2P_{m,\text{LO},\lambda}}{\sigma_{\text{RIN}}^2 + \sigma_{\text{Shot}}^2 + \sigma_{\text{TIA}}^2}. \quad (15)$$

From this $\text{SNR}_{m,\lambda}$ the variance of the measured electrical phase can be calculated. To this end, the m -th line in the measured electrical spectrum Fig. 2(b) is represented by a sinusoidal with frequency $f_m = \Delta f_0 + m\Delta f_{\text{mod}}$. Finite $\text{SNR}_{m,\lambda}$ then leads to a fluctuation of both amplitude and phase of this sinusoidal. These fluctuations are represented by an in-phase component $x = \hat{n} \cos \psi$ and a quadrature component $y = \hat{n} \sin \psi$, where ψ is equally distributed in the interval $0 \dots 2\pi$:

$$V_{m,\lambda} = (\hat{V}_{m,\lambda} + x) \cos(\omega_m t) - y \sin(\omega_m t), \quad x = \hat{n} \cos \psi, \quad y = \hat{n} \sin \psi. \quad (16)$$

The phase $\varphi_{m,\lambda}$ of signal $V_{m,\lambda}$ is determined by $\tan \varphi_{m,\lambda} = y / (\hat{V}_{m,\lambda} + x)$, which can be approximated by $\tan \varphi_{m,\lambda} \approx y / \hat{V}_{m,\lambda} \approx \varphi_{m,\lambda}$ because $x \ll \hat{V}_{m,\lambda}$ and $y \ll \hat{V}_{m,\lambda}$ for a large $\text{SNR}_{m,\lambda}$. The noise components are unbiased and equal in variance, $x^2 = y^2 = \sigma_{\text{tot}}^2$, therefore the phase variance becomes [43]

$$\sigma_{\varphi,m,\lambda}^2 = \frac{\overline{y^2}}{\hat{V}_{m,\lambda}^2} = \frac{\frac{1}{2} \hat{n}^2}{\hat{V}_{m,\lambda}^2} = \frac{\sigma_{\text{tot}}^2}{\hat{V}_{m,\lambda}^2} = \frac{1}{2 \times \text{SNR}_{m,\lambda}}. \quad (17)$$

The phase variance for the IF lines as detected by Rx_{meas} and Rx_{ref} are then:

$$\sigma_{\varphi,m,\lambda,\text{meas}}^2 = \frac{1}{2 \times \text{SNR}_{m,\lambda,\text{meas}}}, \quad \sigma_{\varphi,m,\lambda,\text{ref}}^2 = \frac{1}{2 \times \text{SNR}_{m,\lambda,\text{ref}}}. \quad (18)$$

The signal-to-noise power ratios $\text{SNR}_{m,\lambda,\text{meas}}$ and $\text{SNR}_{m,\lambda,\text{ref}}$ are found by substituting in Eq. (15) $P_{m,\text{sig},\lambda}$, $P_{m,\text{LO},\lambda}$ by $P_{m,\text{sig},\lambda,\text{meas}}$, $P_{m,\text{LO},\lambda,\text{meas}}$, and $P_{m,\text{sig},\lambda,\text{ref}}$, $P_{m,\text{LO},\lambda,\text{ref}}$, respectively.

3.4 Impact of stochastic crosstalk

For low backscattered power levels, the measurement precision is limited by crosstalk via the finite isolation of the 3 dB output coupler CPL3 in Fig. 1, which is used to couple the light to and from the sensor head, see Fig. 6. For the coupler used in our experiments, the crosstalk amounts to $\Gamma = E_{\text{sig,cross}} / E_{\text{sig,in}}$, $\Gamma_{\text{dB}} = 20 \lg \Gamma = -57 \text{ dB}$. The input component of the electric field is denoted by $E_{\text{sig,in}}$, and the crosstalk component by $E_{\text{sig,cross}} = \Gamma E_{\text{sig,in}}$.

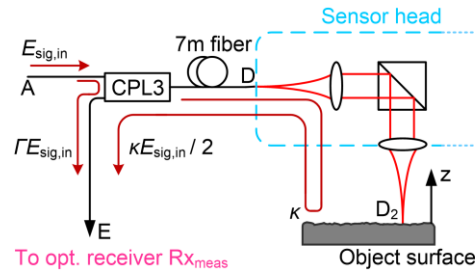


Fig. 6. The signal field $E_{\text{sig,in}}$ at point A is coupled to the sensor head via the 3 dB coupler CPL3. The field is reflected at the object surface with an amplitude reflection coefficient κ , and the reflected field $\kappa E_{\text{sig,in}}/2$ is redirected to the optical receiver $R_{\text{x,meas}}$. A small portion $\Gamma E_{\text{sig,in}}$ of the input light propagates directly to $R_{\text{x,meas}}$ due to the finite isolation Γ of coupler CPL3. For a precise measurement, $\kappa/2 \gg \Gamma$ should hold.

The actual signal component $E_{\text{sig,out}} = \kappa E_{\text{sig,in}}/2$ includes the $1/\sqrt{2}$ coupling factor of the 3dB coupler in the forward and in the backward direction as well as the amplitude reflection coefficient κ associated with the sensor head and the object surface.

In the following, we denote the optical path length from CPL3 through the 7 m long fiber leading to the sensor head and back to CPL3 (path CPL3-D-CPL3 in Fig. 1) as $D_{2 \times 7\text{m}}$. The optical path length for the signal component is denoted as D_z (path A-CPL3-D-D₂-D-CPL3-E). The optical path length D_{cross} (path A-CPL3-E) for the crosstalk component can then be expressed by $D_{\text{cross}} = D_z - D_{2 \times 7\text{m}} - 2z$. The amplitude of each comb line m arriving at the detector is a superposition of the actual signal component and the crosstalk:

$$E_{m,\text{sig}}(\omega_m) = \hat{E}_{m,\text{sig,in}} \Re \left\{ \frac{1}{2} \kappa \exp \left(j \left(\omega_m t - D_z \frac{\omega_m}{c} \right) \right) + \Gamma \exp \left(j \left(\omega_m t - D_{\text{cross}} \frac{\omega_m}{c} \right) \right) \right\}. \quad (19)$$

With the auxiliary relations:

$$x' = \Gamma \cos \left(\left(D_{2 \times 7\text{m}} + 2z \right) \frac{\omega_m}{c} \right) \quad y' = \Gamma \sin \left(\left(D_{2 \times 7\text{m}} + 2z \right) \frac{\omega_m}{c} \right), \quad (20)$$

we can simplify Eq. (19) and write in analogy to Eq. (16):

$$\frac{E_{m,\text{sig}}(\omega_m)}{\hat{E}_{m,\text{sig,in}}} = \left(\frac{1}{2} \kappa + x' \right) \cos \left(\omega_m t - D_z \frac{\omega_m}{c} \right) - y' \sin \left(\omega_m t - D_z \frac{\omega_m}{c} \right). \quad (21)$$

Our calibration measurement compensates any fluctuations in the optical path length D_z . The in-phase crosstalk $x' \ll \frac{1}{2} \kappa$ is a small contribution, but the quadrature crosstalk y' leads to a phase error $\tan \varphi_{m,\text{cross}} \approx y' / (\kappa/2) \approx \varphi_{m,\text{cross}}$. Without stochastic fluctuations of the path length $D_{2 \times 7\text{m}}$, this systematic error is λ -periodic when changing $2z$, $\varphi_{m,\text{cross}} \approx \frac{\Gamma}{\kappa/2} \sin \left(\left(D_{2 \times 7\text{m}} + 2z \right) \omega_m / c \right)$, and is called cyclic error [44]. However, due to thermal fluctuations of the fiber path length $D_{2 \times 7\text{m}}$, the phases of x' and y' in Eq. (20) vary randomly on the time scale of environmental thermal fluctuations. Considering the first term in Eq. (19) as signal and the second term as noise, we define a cross-talk related signal-to-noise power ratio:

$$\text{SNR}_{\text{cross}} = \frac{\left(\frac{1}{2} \kappa \right)^2}{\frac{1}{2} \Gamma^2} = \frac{(\kappa/2)^2}{\Gamma^2}. \quad (22)$$

In our experiments, we measure the object distance z with a sampling rate of 3.3kHz and evaluate the mean and the variance of this distance by averaging over 1,000 samples. This corresponds to an observation time of $1000/3.3\text{kHz} = 303\text{ms}$. The cross-talk related variance of these measurements is hence dominated by fluctuations with bandwidths bigger than $1/(2 \times 303\text{ms}) = 3.3\text{kHz}/(2 \times 1000) = 1.65\text{Hz}$ and smaller than $3.3\text{kHz}/2 = 1.65\text{kHz}$.

Typical spectra of stochastic room temperature fluctuations cover a range up to 4 Hz [35]. For frequencies from 1.65Hz up to 4Hz the standard deviation of the room temperature is approximately $\sigma_T = 5\text{mK}$. The dynamic thermal response of a standard Hytel jacketed singlemode optical fiber has a 3 dB bandwidth of roughly 10 Hz [45] and reacts much faster than the room temperature can fluctuate. With a geometrical path length $L = 2 \times 7\text{m}$ for $D_{2 \times 7\text{m}}$, and with the relation $dD_{2 \times 7\text{m}}/(LdT) \approx 11\mu\text{m}/(\text{K m})$ from Eq. (5), the effective optical path length fluctuation during the observation time is of the order $\sigma_{D_{2 \times 7\text{m}}} = dD_{2 \times 7\text{m}}/(LdT)L\sigma_T = 0.8\mu\text{m}$. For simplicity, we approximate the Gaussian probability density function (pdf) for the randomly changing optical path length $D_{2 \times 7\text{m}}$ by a rectangular pdf with a width of $2\sigma_{D_{2 \times 7\text{m}}} = 1.6\mu\text{m}$, centered at the expectation value $\langle D_{2 \times 7\text{m}} \rangle$. With an object wavelength of $\lambda_m = 2\pi c/\omega_m = 1.55\mu\text{m}$, the phase terms $2\pi D_{2 \times 7\text{m}}/\lambda_m$ of x' and y' are equally distributed in the interval $0 \dots 2\pi$, and we can proceed in analogy to Eq. (17). The phase variance due to stochastic crosstalk is therefore:

$$\sigma_{\varphi,m,\text{cross}}^2 = \frac{1}{2 \times \text{SNR}_{\text{cross}}} \quad \text{for } \Gamma \ll \frac{\kappa}{2}. \quad (23)$$

For the calibration wavelength, the reflection coefficient κ of the calibration mirror is so large that the crosstalk influence can be neglected.

3.5 Calculation of the distance uncertainty from the phase variances

The measured distance is calculated from the slope $d\Delta\varphi_m/dm$ of the phase differences between measurement and reference signal, see Eq. (4). The phase fluctuation of the m -th IF line pair with a standard deviation $\sigma_{\Delta\varphi,m,\lambda}$ comprises contributions originating from both IF lines as seen by Rx_{meas} and by Rx_{ref} , see Eq. (18), and from the crosstalk as specified in Eq. (23). Because these three random processes are uncorrelated, the respective variances are to be added:

$$\sigma_{\Delta\varphi,m,\lambda}^2 = \sigma_{\varphi,m,\lambda,\text{meas}}^2 + \sigma_{\varphi,m,\lambda,\text{ref}}^2 + \sigma_{\varphi,m,\text{cross}}^2 := \sigma_{\Delta\varphi,\lambda}^2. \quad (24)$$

If we assume spectrally perfectly flat combs, the SNR is the same for each line m , and therefore all lines have the same variance $\sigma_{\Delta\varphi,\lambda}^2$ of the phase difference. To obtain the slope, a linear regression is used. From the analytic formula for the slope uncertainty of a linear regression [46], the variance of the measured distance z at center wavelength λ can be calculated when using a number of N comb lines:

$$\sigma_{z,\lambda}^2 = \frac{\sigma_{\Delta\varphi,\lambda}^2}{N} \frac{3}{(\omega_{\text{mod,sig}}/c)^2 (N^2 - 1)}, \quad (25)$$

The evaluation of $N = 7$ comb lines with $f_{\text{mod,sig}} = 40\text{GHz}$ corresponds to the interrogation of an optical spectrum with 240 GHz bandwidth. It is a key feature of the dual comb-based heterodyne detection that robust and inexpensive low-frequency (<200 MHz) electronic detection is sufficient for high-precision distance measurement, while exploiting optical bandwidths of hundreds or even thousands of GHz. To fully understand the system capabilities and limitations, we use a numerical model considering that the combs are not spectrally flat. Measurement results together with calculated data are plotted in Fig. 7.

The standard deviations of both individual measurements $\sigma_{z,obj}$ and $\sigma_{z,cal}$ as well as the standard deviation of the temperature-compensated measurement $\sigma_{z,comp}$ are plotted as a function of reflection coefficient $\kappa_{dB} = 20\lg \kappa$ for the 1550 nm signal comb (total power -2.5 dBm at point D in Fig. 1). The standard deviation $\sigma_{z,obj}$ of the distance measurement to the object surface decreases with an increasing reflection coefficient κ , while the standard deviation $\sigma_{z,cal}$ of the measured distance to the calibration mirror remains essentially constant. The results of the compensated distance measurements (red circles) confirm the theoretical prediction (solid line) according to Section 3.3. The parameters used for the calculations are listed in Appendix E. For large reflection coefficients of the object surface, the precision of the compensated measurement is limited by the uncertainty of the calibration measurement. The high uncertainty of the calibration measurement results from the fact that the comb generators see a higher modulator insertion loss at 1300 nm. For small reflection coefficients, the object measurement dominates the uncertainty of the compensated measurement. A detailed analysis of the effect of the distribution of optical power between object and calibration measurement can be found in Appendix F. Nevertheless, the reflection coefficient has a dynamic range of 20 dB for a standard deviation of distance measurements below $8 \mu\text{m}$. Therefore the distance to a large variety of surfaces can be measured accurately. For characterization independent of speckle-induced phase noise, which depends on the specific surface roughness, a mirror was used as a measurement target for the measurements presented in Fig. 7. Measurements to optically rough surfaces include an additional error due to speckle-induced phase noise with a magnitude depending on the surface characteristics [23,47,48].

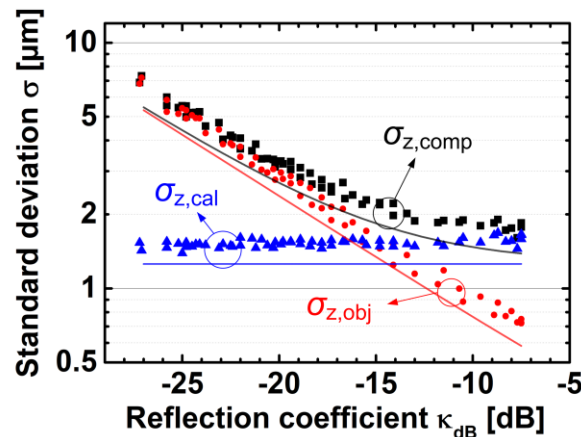


Fig. 7. Standard deviation of distance measurements (filled symbols) and theoretical curves (solid lines, from Sect. 3.3) as a function of the reflection coefficient $\kappa_{dB} = 20\lg \kappa$ for the 1550 nm signal comb. The theoretical curves were obtained from calculations that are based on measured shapes of the comb spectra. For the 1550 nm signal comb, the total emitted signal comb power is -2.5 dBm at point D in Fig. 1. Noise and temperature fluctuations dictate the standard deviations for the distance measurements at the object wavelength (red, $\sigma_{z,obj}$) and at the calibration wavelength (blue, $\sigma_{z,cal}$). The standard deviation decreases with an increasing reflection coefficient when measuring at the object wavelength, while the return path for the calibration wavelength and therefore the measured standard deviation remains essentially constant. However, because there is less power available for the calibration measurement, we find that $\sigma_{z,cal} > \sigma_{z,obj}$ for a high reflection coefficient in the object path. The variance $\sigma_{z,comp}^2$ for the compensated distance measurement results from adding the variances $\sigma_{z,obj}^2$ and $\sigma_{z,cal}^2$. The smallest standard deviation is $\sigma_{z,comp} = 2 \mu\text{m}$ and is dominated by the standard deviation of the calibration measurement.

3.6 Performance comparison with the state-of-the-art

In addition to measurement accuracy, the time needed for one measurement is an important parameter, especially if motion blur should be avoided when scanning an object by moving a measurement spot over its surface, or if fast and dense sample digitization is required. A compilation of standard deviations σ and measurement times τ for published comb-based distance measurement systems is plotted in Fig. 8. The dashed line represents the relation $\sigma = p\tau^{-1/2}$ for averaging statistically independent noisy samples. The proportionality factor p is determined by our experimental data denoted by a red star \star . Measurement systems with smaller p lie below the dashed line and have a smaller standard deviation for a given measurement time. System [1] excels in terms of precision, but at the cost of an elaborate setup: Two MLL frequency combs are used, which are phase-locked to achieve linewidths of a few Hertz, and the accuracy of the synthetic-wavelength interferometry is improved by an additional interferometric measurement, which is only possible for mirror-like flat object surfaces. System [15] achieves an impressively small measurement time, again at the cost of setup complexity: The system comprises two parametric comb generators, each with one phase modulator, two injection-locked laser diodes, wavelength-division multiplexing splitters and combiners, two high-power fiber amplifiers, and multiple nonlinear and linear fiber sections. Recently, in system [17], two broadband Kerr combs and high-frequency detection electronics have been utilized to achieve an impressive combination of small measurement time and high precision. However, the generation of two Kerr comb involves complicated setups with high power optical amplifiers and the utilized high-frequency detection electronics are prohibitively expensive for many industrial applications. In contrast to that, our demonstration relies on a comparatively simple concept that only comprises electro-optic modulators and the associated drive circuitry, enabling detection and data processing with relatively low-frequency electronics, and is amenable to photonic integration [49–51].

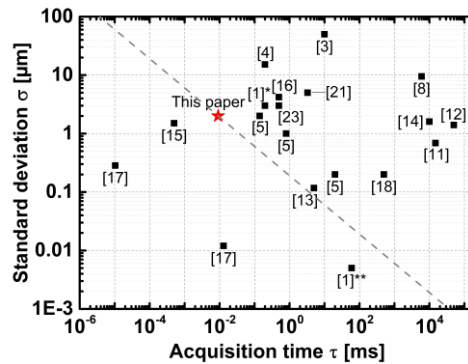


Fig. 8. Standard deviation σ of distance measurement and acquisition time τ in a double-logarithmic display for published comb-based distance measurement systems exploiting synthetic-wavelength interferometry. The dashed line represents the relation $\sigma = p\tau^{-1/2}$ for averaging statistically independent noisy samples. The proportionality factor $p = 2\mu\text{m}\sqrt{9.1\mu\text{s}} = 6 \times 10^{-9} \text{ms}^{1/2}$ is determined by our experimental data (label \star , $\sigma = 2\mu\text{m}$, $\tau = 9.1\mu\text{s}$). Demonstrations with smaller p are found below the dashed line and have a smaller standard deviation for a given measurement time. Demonstration [1]** stands out due to a standard deviation of 5 nm at 60 ms acquisition time, which was achieved by combining SWI with classical optical interferometry at a single comb tone. Considering the SWI part only, the standard deviation of demonstration [1] amounts to 3 μm at 0.2 ms acquisition time, indicated by data point [1]*. Considering pure SWI measurements only, our experiment outperforms all previous demonstrations except for [15] and [17], both of which relied on broadband parametric combs with associated complex setups.

4. Experimental demonstrations

4.1 Outlier removal

The slope $d\Delta\varphi_m/dm$ for determining the distance is calculated from a linear regression model. This allows the implementation of a robust distance outlier removal: The two parameters of a linear regression model are determined by minimizing the squared differences between measured phase values $\Delta\varphi_m$ and the model values $\Delta\Phi_m$. The quality of the fit is quantified with the coefficient of determination $r^2 = 1 - SS_{\text{res}}/SS_{\text{tot}}$, which is specified by the sum of the squared errors $SS_{\text{res}} = \sum_m (\Delta\varphi_m - \Delta\Phi_m)^2$ between measurements and model, and by the sum of the squared deviations $SS_{\text{tot}} = \sum_m (\Delta\varphi_m - \overline{\Delta\varphi_m})^2$ of the measurements from the mean $\overline{\Delta\varphi_m}$. Setting a suitable threshold to r^2 allows the removal of outliers, which may, e.g., be caused by particularly noisy phase measurements in case of a small object reflection κ , or by phase unwrapping errors.

We demonstrate the viability of the outlier removal technique for an extreme case with large reflected power variations. To this end, we use an ordinary printed-circuit board as depicted in Fig. 9(a) as a test sample and scan its surface topography along a line indicated as x . The sensor is moved with the help of a CMM and is kept at a constant height. The variety of surface types, the surface height variations, and the limited depth of field ($300\ \mu\text{m}$) of our objective lens lead to large variations of the reflected optical power and therefore to uncertainties in the measured height profile. Moreover, the measured distances cover almost the whole of the unambiguity range of $3.7\ \text{mm}$, making unwrapping errors of the noisy phases more likely at the edges of the unambiguity range. This leads to a significant number of outliers as can be seen in Fig. 9(b), which shows the raw data (black filled circles) of the height profile along an x -directed scan in Fig. 9(a). However, if we consider only the subset of data points which leads to a coefficient of determination $r^2 \geq 0.99$, a clean height profile can be extracted, see red dots in Fig. 9(b). This is also to be seen when comparing the fussy display of the raw data in Fig. 9(c) with the crisp display in Fig. 9(d) where almost 50% of the data points were removed as outliers. In practice, the number of outliers is not as extreme, because the CMM adaptively adjusts the sensor height with respect to the surface according to the measured distance, thereby avoiding disadvantageous defocusing and measurements at the edge of the unambiguity range. Lateral scanning is stopped during height adjustments and continued after the height has been adjusted to within a chosen range interval above the surface. This procedure avoids the acquisition of range data with additional potential errors caused by simultaneous movement in z -direction and range data acquisition. By operating close to the focal length of the objective lens, the amount of collected back-scattered light is maximized, which increases the obtained SNR, thus improving the measurement precision, as analyzed in Section 3.3 – 3.5.

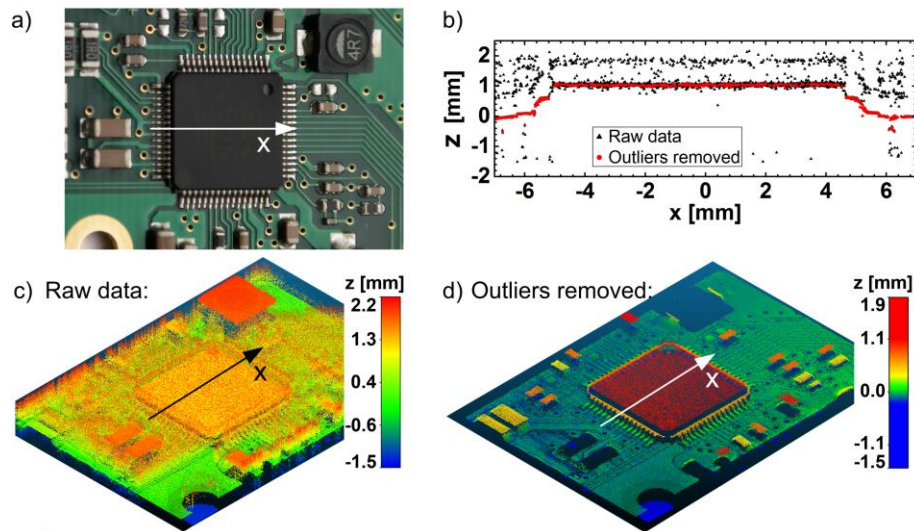


Fig. 9. Demonstration of outlier removal. (a) Photograph of a printed-circuit board (PCB), comprising a variety of surfaces including an integrated circuit (IC) with a black polymer package. (b) Height profile of the sample along a line in x -direction, across the black package of the IC, see Subfigure (a). Black: Raw data. Red: Data after outlier removal. (c) Color-coded surface profile with 1.5 million measurement points resulting from a measurement scan without outlier removal. (d) Color-coded surface profile after outlier removal, comprising 0.8×10^6 measurement points with an r^2 better than the threshold 0.99.

4.2 Verification by tactile measurements

To confirm the accuracy of our distance measurement scheme, we compare optical profile measurements of steps in milled aluminum blocks with tactile reference measurements. Also here, we used the outlier removal technique described in the previous section. For scanning we use again a CMM (Carl Zeiss O-Inspect 442 with VAST XXT probe) with a maximum scanning speed of 300 mm/s in x - and y -direction and 100 mm/s in z -direction. For tactile height measurements, the system has a maximum permissible probing error $MPE_P = 1.9 \mu\text{m}$ [52,53]. Five samples were prepared with typical surface treatments encountered in industrial applications to provide exemplary results for a variety of surfaces, see Fig. 10(a). The surface profile is measured along a line (x -axis) across the first five steps #1,#2, ..., #5, taking 60 measurements with the tactile probe and 40,000 measurements with the optical sensor, see Fig. 10(b). The differences between the averaged optical sensor values \bar{z}_{opt} and the averaged mechanically measured values \bar{z}_{tact} are plotted in Fig. 10(d) for each step surface. For all samples, these differences are in the range of a few micrometers only. A full 3D point cloud from optical measurements is shown in Fig. 10(c), showing clearly the topography of the “KIT IPQ” engraving.

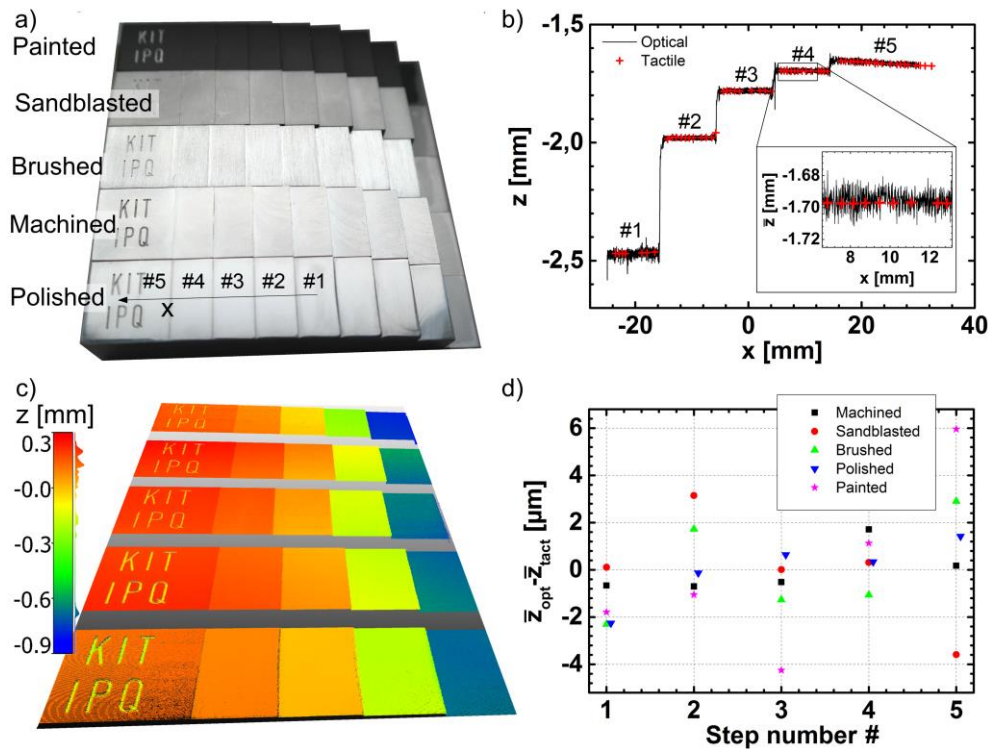


Fig. 10. Comparison of optical measurements to tactile reference measurements. (a) Photograph of steps milled in an aluminum block and prepared with different surface treatments. (b) Scan along the line marked by the arrow on the polished sample. Optical measurements (black) and tactile measurements (red) agree well. Tactile measurements were performed with an industrial coordinate measuring machine (CMM). (c) Color-coded surface profiles of the samples shown in (a), 5.1×10^6 points in total. The measurements show clearly the topography of the “KIT IPQ” engraving (d) Differences of mean values of optical (\bar{z}_{opt}) and of tactile measurements (\bar{z}_{tact}) for each step. For all samples, these differences are in the range of a few micrometers.

4.3 Application examples

In this section we give two more examples for surface profile measurements. In Fig. 11, a photograph and the measured height profile of the backside of a 20 Euro-cent coin are shown. The waist radius $8.7 \mu\text{m}$ of our measurement beam together with the high mechanical resolution of the CMM allows to resolve fine details that are not accessible with a conventional tactile measurement system. Another example is shown in Fig. 12, where the photograph of a used bullet casing together with the height profile scan is depicted. The dent made by the firing pin can be seen clearly. Imperfections of the firing pin geometry leave characteristic marks on the bullet casing which may be used in forensic studies to identify the gun that was used to fire the bullet [54–56]. The inset in Fig. 12 provides a zoomed view of a volume, detailing a cross section through the indentation. Our outlier removal technique described in Section 4.1 leads to less densely sampled regions, where a high angle of incidence together with the specular surface characteristics of the specific sample are the cause of low returned power levels. Only reliable measurement points are recorded. The high accuracy of the measured height profile paves the road for an application in other fields such as in forensics.

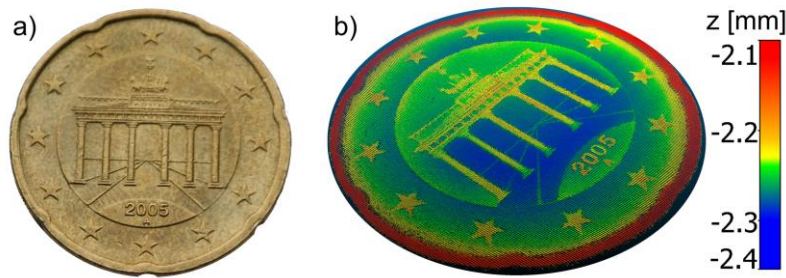


Fig. 11. Surface topography measurements of a 20 Euro-cent coin. (a) Photograph of the coin. (b) Color-coded surface profile with 0.7×10^6 points resulting from a scanning optical topography measurement.

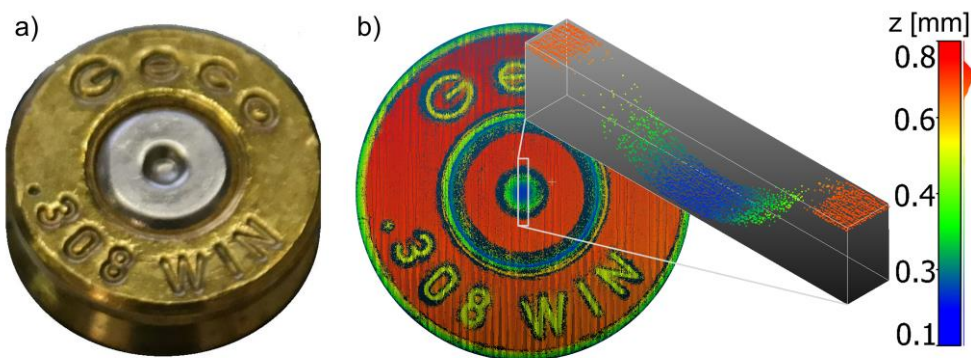


Fig. 12. Surface topography measurements. (a) Photograph of the backside of a used bullet casing. (b) Color-coded surface profile with 0.6×10^6 points resulting from a scanning optical topography measurement. Inset: Zoomed view of a volume, detailing a cross section through the indentation caused by the firing pin.

5. Summary and conclusion

We have demonstrated a robust, technically straightforward, and yet precise comb-based distance measurement concept based on dual-color modulator-generated frequency combs. The technique can maintain its precision even under realistic industrial boundary conditions. An acquisition time of $9.1 \mu\text{s}$ per point avoids motion blur. We have further introduced a compensation scheme that eliminates temperature-induced drift of the fiber optic components and thus permits placement of critical optical and electronic components many meters remote from the sensor head. This scheme enables operation of the sensor on a coordinate measuring machine and is key to deploying the technique in a harsh industrial environment. To the best of our knowledge, our experiments represent the first demonstration of dead-zone-free drift compensation for comb-based distance measurements through optical fibers. In the current implementation, measured distances are output at a rate of 3.3 kHz, which allows a rapid recording of a large numbers of points while continuously scanning the sensor head. We demonstrate the viability of the concept by height profile measurements on a wide range of samples, where we achieve precisions in the single-digit micrometer regime.

Appendix A: Multi-heterodyne detection

In the following section, we give a rigorous mathematical description of the measurement scheme, which relies on quadratic detection of detuned frequency combs (FC) by the measurement and reference detector. Analytical signals $\underline{E}(t)$ are used to describe the time-domain electric fields, with the real part of the analytical signal representing the physically relevant field,

$E(t) = \Re\{\underline{E}(t)\}$. The optical power is then given by $P = Z_0^{-1} \langle E^2(t) \rangle$, where $\langle - \rangle$ denotes the average over a few cycles of the optical carrier and $Z_0 = 376.7 \Omega$ represents the wave impedance of free space. For simplicity, we describe here only one set of frequency combs at a single center wavelength λ_{cal} or λ_{obj} . In a first step we consider the measurement detector (Rx_{meas}) only. In accordance to the system detailed in Fig. 1, we consider the complex optical amplitudes $\underline{E}_{\text{sig,meas}}$ for the signal comb arriving at the measurement detector. Each signal comb line l has an (angular) optical frequency $\omega_{l,\text{sig}}$,

$$\omega_{l,\text{sig}} = \omega_{0,\text{sig}} + l\omega_{\text{mod,sig}}. \quad (26)$$

The amplitudes of the signal comb lines are denoted as $\hat{E}_{l,\text{sig,meas}}$, and the associated optical path length to the detector amounts to $2z + D_{\text{sig,meas}}$, where $D_{\text{sig,meas}}$ denotes the optical path length through the measurement setup to and from the origin $z = 0$ of the measurement coordinate system, see Fig. 1. Similarly, the complex optical amplitudes of the LO comb at the measurement detector are denoted as $\underline{E}_{\text{LO,meas}}$, and each comb line m has an (angular) optical frequency $\omega_{m,\text{LO}}$,

$$\omega_{m,\text{LO}} = \omega_{0,\text{LO}} + m\omega_{\text{mod,LO}} = (\omega_{0,\text{sig}} + \Delta\omega_0) + m(\omega_{\text{mod,sig}} + \Delta\omega_{\text{mod}}) \quad (27)$$

with a center frequency detuning $\Delta\omega_0$, a detuning of the line spacing of $\Delta\omega_{\text{mod}}$, and an amplitude $\hat{E}_{m,\text{LO,meas}}$. The LO comb arrives at the measurement detector after propagation over the optical path length $D_{\text{LO,meas}}$, which is entirely located within the measurement setup. The complex amplitudes of the two FC at the measurement detector are then given as

$$\begin{aligned} \underline{E}_{\text{sig,meas}}(t) &= \sum_l \hat{E}_{l,\text{sig,meas}} \exp(j\omega_{l,\text{sig}}t) \exp(-j(2z + D_{\text{sig,meas}})\omega_{l,\text{sig}}/c) \\ \underline{E}_{\text{LO,meas}}(t) &= \sum_m \hat{E}_{m,\text{LO,meas}} \exp(j\omega_{m,\text{LO}}t) \exp(-jD_{\text{LO,meas}}\omega_{m,\text{LO}}/c). \end{aligned} \quad (28)$$

The superposition of the signal and LO comb on perfectly balanced photodetectors (BD) with sensitivity S leads to a photocurrent containing multiple IF tones. The photocurrent i_{meas} of the measurement detector is given by

$$\begin{aligned} i_{\text{meas}}(t) &= Z_0^{-1} S \cdot \Re\left\{ \underline{E}_{\text{sig,meas}}(t)^* \underline{E}_{\text{LO,meas}}(t) \right\} \\ &= Z_0^{-1} S \cdot \Re\left\{ \sum_l \sum_m \hat{E}_{l,\text{sig,meas}} \hat{E}_{m,\text{LO,meas}} \right. \\ &\quad \cdot \exp\left(j(\Delta\omega_0 + (m-l)\omega_{\text{mod,sig}} + m\Delta\omega_{\text{mod}})t\right) \\ &\quad \left. \cdot \exp\left(j\left((2z + D_{\text{sig,meas}})\omega_{l,\text{sig}} - D_{\text{LO,meas}}\omega_{m,\text{LO}}\right)/c\right) \right\}. \end{aligned} \quad (29)$$

The photocurrent i_{ref} of the reference detector can be derived in an analogous way by replacing “meas” by “ref” in the subscripts,

$$\begin{aligned} i_{\text{ref}}(t) &= Z_0^{-1} S \cdot \Re\left\{ \underline{E}_{\text{sig,ref}}(t)^* \underline{E}_{\text{LO,ref}}(t) \right\} \\ &= Z_0^{-1} S \cdot \Re\left\{ \sum_l \sum_m \hat{E}_{l,\text{sig,ref}} \hat{E}_{m,\text{LO,ref}} \right. \\ &\quad \cdot \exp\left(j(\Delta\omega_0 + (m-l)\omega_{\text{mod,sig}} + m\Delta\omega_{\text{mod}})t\right) \\ &\quad \left. \cdot \exp\left(j\left(D_{\text{sig,ref}}\omega_{l,\text{sig}} - D_{\text{LO,ref}}\omega_{m,\text{LO}}\right)/c\right) \right\}. \end{aligned} \quad (30)$$

In this relation, the quantities $D_{\text{sig,ref}}$ and $D_{\text{LO,ref}}$ denote the optical path lengths between the respective comb source and the reference detector.

The frequency detunings $\Delta f_0 = \Delta\omega_0/(2\pi)$ and $\Delta f_{\text{mod}} = \Delta\omega_{\text{mod}}/(2\pi)$ amount to tens of megahertz and are small compared to the line spacing $\omega_{\text{mod,sig}}$ of roughly 40 GHz. In theory, the photocurrent spectrum shows beat signals at distinct intermediate frequencies $f_{m,l}$,

$$f_{m,l} = \left| \Delta f_0 + (m-l)f_{\text{mod,sig}} + m\Delta f_{\text{mod}} \right|. \quad (31)$$

However, only a subset of these lines can actually be acquired by the photodetector and the subsequent A/D converter. For the FC deployed in our experiments, the analog bandwidth B of the photodetectors amounts to 350 MHz and is much smaller than the ~40 GHz line spacing of the frequency combs, $B \ll f_{\text{mod,sig}} \approx f_{\text{mod,LO}}$. Moreover, the number of comb lines is limited such that $m\Delta f_{\text{mod,LO}} \ll f_{\text{mod,sig}} \approx f_{\text{mod,LO}}$ for all comb line indices m .

As a consequence, for a given LO comb line m , only the beat note with the corresponding signal comb of same index $m = l$ is visible in the photocurrent. IF lines are hence found at distinct frequencies $f_{\text{IF},m} = \left| \Delta f_0 + m\Delta f_{\text{mod}} \right|$. These signals are amplified by a transimpedance amplifier with a transimpedance of R_{TIA} . The resulting voltage signal $V_{\text{meas}}(t)$ at the measurement detector is then given as

$$V_{\text{meas}}(t) = \sum_m \hat{V}_{m,\text{meas}} \cos\left((\Delta\omega_0 + m\Delta\omega_{\text{mod}})t + \varphi_{m,\text{meas}}\right), \quad (32)$$

$$\hat{V}_{m,\text{meas}} = SR_{\text{TIA}} \sqrt{2P_{m,\text{sig,meas}} 2P_{m,\text{LO,meas}}}.$$

The corresponding phases $\varphi_{m,\text{meas}}$ of the IF lines at the measurement detector can be derived from Eq. (29),

$$\begin{aligned} \varphi_{m,\text{meas}}(2z + D_{\text{sig,meas}}, D_{\text{LO,meas}}) &= \left((2z + D_{\text{sig,meas}})\omega_{m,\text{sig}} - D_{\text{LO,meas}}\omega_{m,\text{LO}} \right) / c \\ &= \left((2z + D_{\text{sig,meas}}) - D_{\text{LO,meas}} \right) (\omega_{0,\text{sig}} + m\omega_{\text{mod,sig}}) / c \\ &\quad - D_{\text{LO,meas}} (\Delta\omega_0 + m\Delta\omega_{\text{mod}}) / c \\ &= 2\pi \left((2z + D_{\text{sig,meas}}) - D_{\text{LO,meas}} \right) \Lambda_m^{-1} \\ &\quad + 2\pi \left((2z + D_{\text{sig,meas}}) - D_{\text{LO,meas}} \right) \lambda_{0,\text{sig}}^{-1} \\ &\quad - D_{\text{LO,meas}} (\Delta\omega_0 + m\Delta\omega_{\text{mod}}) / c. \end{aligned} \quad (33)$$

The last part of Eq. (33) contains the so-called synthetic wavelength

$$\Lambda_m = c \left(m f_{\text{mod,sig}} \right)^{-1} \quad (34)$$

and shows the relation to classical interferometry with a single optical wavelength λ , where the phase shift φ experienced by an optical signal after propagation over the optical path length D is determined by $\varphi = 2\pi D \lambda^{-1}$.

The beat signals at the reference detector have the exactly same frequencies as the beat signals at the measurement detector and serve as phase references. Their phases are determined analogously to Eq. (33) and are given as

$$\varphi_{m,\text{ref}}(D_{\text{sig,ref}}, D_{\text{LO,ref}}) = \left(D_{\text{sig,ref}}\omega_{m,\text{sig}} - D_{\text{LO,ref}}\omega_{m,\text{LO}} \right) / c \quad (35)$$

The phase differences of the various beat signals are given by:

$$\begin{aligned}
\Delta\varphi_m(z) &= \varphi_{m,\text{meas}}(2z + D_{\text{sig,meas}}, D_{\text{LO,meas}}) - \varphi_{m,\text{ref}}(D_{\text{sig,ref}}, D_{\text{LO,ref}}) \\
&= (2z + D_{\text{sig,meas}} - D_{\text{LO,meas}} - (D_{\text{sig,ref}} - D_{\text{LO,ref}}))m\omega_{\text{mod,sig}}/c \\
&\quad + (2z + D_{\text{sig,meas}} - D_{\text{LO,meas}} - (D_{\text{sig,ref}} - D_{\text{LO,ref}}))\omega_{0,\text{sig}}/c \\
&\quad - (D_{\text{LO,meas}} - D_{\text{LO,ref}})\Delta\omega_0/c \\
&\quad - (D_{\text{LO,meas}} - D_{\text{LO,ref}})m\Delta\omega_{\text{mod}}/c.
\end{aligned} \tag{36}$$

The distance information is extracted from evaluating the slope of the unwrapped phase differences $\Delta\varphi_m(z)$ as a function of the comb line index m . This slope is given by

$$\begin{aligned}
\frac{d\Delta\varphi_m(z)}{dm} &= \frac{\omega_{\text{mod,sig}}}{c} (2z + D_{\text{sig,meas}} - D_{\text{LO,meas}} - D_{\text{sig,ref}} + D_{\text{LO,ref}}) \\
&\quad - \frac{\Delta\omega_{\text{mod}}}{c} (D_{\text{LO,meas}} - D_{\text{LO,ref}})
\end{aligned} \tag{37}$$

If the optical path lengths inside the fiber was constant, all terms containing $D_{\text{sig,meas}}, D_{\text{LO,meas}}, D_{\text{sig,ref}}$ and $D_{\text{LO,ref}}$ in Eq. (37) could be eliminated by a simple calibration to an arbitrary zero point z_0 by subtracting a constant offset such that $d\Delta\varphi_m(z_0=0)/dm = 0$. For any other distance, the quantity $z - z_0$ could then be determined accurately from the measured slope as $\omega_{\text{mod,sig}}$ and c are precisely known. However, due to temperature fluctuations of the setup and the optical fibers, the various optical path lengths change by $\Delta D_{\text{sig,meas}}, \Delta D_{\text{LO,meas}}, \Delta D_{\text{sig,ref}}$ and $\Delta D_{\text{LO,ref}}$ within a time of $t - t_0$, see Eq. (1). The difference of the slope with respect to $z_0 = 0, t_0 = 0$ is then given by

$$\begin{aligned}
&\frac{d\Delta\varphi_m(z,t)}{dm} - \frac{d\Delta\varphi_m(z_0=0,t_0=0)}{dm} \\
&= \frac{\omega_{\text{mod,sig}}}{c} (2z + \Delta D_{\text{sig,meas}} - \Delta D_{\text{LO,meas}} - (\Delta D_{\text{sig,ref}} - \Delta D_{\text{LO,ref}})) \\
&\quad - \frac{\Delta\omega_{\text{mod}}}{c} (\Delta D_{\text{LO,meas}} - \Delta D_{\text{LO,ref}}). \\
&\cong \frac{\omega_{\text{mod,sig}}}{c} (2z + \Delta D_{\text{sig,meas}} - \Delta D_{\text{LO,meas}} - (\Delta D_{\text{sig,ref}} - \Delta D_{\text{LO,ref}})).
\end{aligned} \tag{38}$$

The third line in Eq. (38) can be neglected, as $\Delta\omega_{\text{mod}} \ll \omega_{\text{mod,sig}}$ holds, and because for a typical fiber installation $|\Delta D_{\text{LO,meas}} - \Delta D_{\text{LO,ref}}| \ll |\Delta D_{\text{sig,meas}} - \Delta D_{\text{LO,meas}} - (\Delta D_{\text{sig,ref}} - \Delta D_{\text{LO,ref}})|$ is true.

Appendix B: Balanced detection in the presence of noise

In the following section, we analyze the influence of relative intensity noise (RIN) in the balanced reception scheme. Using a signal representation as in Eq. (16), the RIN is treated as a complex noise component $\underline{N}(t) = x''(t) + jy''(t)$ with a real in-phase noise component $x''(t)$ and a real quadrature noise component $y''(t)$. The noise is Gaussian, unbiased, $\langle x''(t) \rangle = 0$, $\langle y''(t) \rangle = 0$, and the corresponding variances are $\sigma_{x''}^2 = \sigma_{y''}^2 = \widehat{w}_{o,\text{RIN}} \Delta f$, where we assume flat optical spectral noise power density of $\widehat{w}_{o,\text{RIN}}$ within the detection bandwidth Δf .

Like the shot noise in Eq. (12), the RIN is determined by the total optical comb powers $P_{\text{sig},\lambda}$ and $P_{\text{LO},\lambda}$ [57]. The detection process is thus treated as heterodyne reception of a monochromatic signal with a monochromatic LO, each with an optical power equal to the corresponding total optical comb power. Signal and LO field are derived from the same source, but are decorrelated with respect to the $\text{RIN}(f)$ -bandwidth of $B = 1\text{GHz}$ by a spatial separation

larger than $c/(nB) = 0.67$ m inside fibers with a refractive index of $n = 1.5$. As a consequence, both contributions are statistically independent. Furthermore, the contributions of both lasers (wavelengths λ_{obj} and λ_{cal}) are statistically independent. For a simpler description, we first consider only a single laser source. The variances of the voltage fluctuations caused by both lasers are then added, see Eq. (11).

The real electric fields of signal and LO, $E_{\text{sig}}(t)$ and $E_{\text{LO}}(t)$, with amplitudes $\hat{E}_{\text{sig,LO}}$ and frequencies $f_{\text{sig,LO}} = \omega_{\text{sig,LO}}/(2\pi)$ are perturbed by the in-phase and quadrature RIN components, $x''_{\text{sig,LO}}(t)$ and $y''_{\text{sig,LO}}(t)$:

$$\begin{aligned} E_{\text{sig}}(t) &= \left[\hat{E}_{\text{sig}} + x''_{\text{sig}}(t) \right] \cos(\omega_{\text{sig}}t) - y''_{\text{sig}}(t) \sin(\omega_{\text{sig}}t) \\ E_{\text{LO}}(t) &= \left[\hat{E}_{\text{LO}} + x''_{\text{LO}}(t) \right] \cos(\omega_{\text{LO}}t) - y''_{\text{LO}}(t) \sin(\omega_{\text{LO}}t). \end{aligned} \quad (39)$$

The fields in Eq. (39) are incident on the two ports of a 3 dB coupler in front of a balanced receiver. Assuming an ideal 3 dB coupler with perfect splitting ratio, the fields $E_{1,2}(t)$ incident on each photodiode 1 and 2 are given as:

$$E_1(t) = \frac{1}{\sqrt{2}}(E_{\text{sig}}(t) - E_{\text{LO}}(t)) \quad E_2(t) = \frac{1}{\sqrt{2}}(E_{\text{sig}}(t) + E_{\text{LO}}(t)). \quad (40)$$

The photocurrents $i_1(t)$ and $i_2(t)$ of each photodiode with a sensitivity S are calculated as

$$i_1(t) = Z_0^{-1} S \langle E_1^2(t) \rangle \quad i_2(t) = Z_0^{-1} S \langle E_2^2(t) \rangle \quad (41)$$

Evaluating Eq. (41) by forming the square, averaging over an optical period and neglecting all terms containing only as small noise contributions, the difference of the photocurrents $i_-(t) = i_2(t) - i_1(t)$ is given as

$$\begin{aligned} i_-(t) = i_2(t) - i_1(t) &= Z_0^{-1} S \left[\hat{E}_{\text{sig}} \hat{E}_{\text{LO}} \cos((\omega_{\text{sig}} - \omega_{\text{LO}})t) \right. \\ &\quad + \hat{E}_{\text{sig}} \left(x''_{\text{LO}}(t) \cos((\omega_{\text{sig}} - \omega_{\text{LO}})t) + y''_{\text{LO}}(t) \sin((\omega_{\text{sig}} - \omega_{\text{LO}})t) \right) \\ &\quad \left. + \hat{E}_{\text{LO}} \left(x''_{\text{sig}}(t) \cos((\omega_{\text{sig}} - \omega_{\text{LO}})t) - y''_{\text{sig}}(t) \sin((\omega_{\text{sig}} - \omega_{\text{LO}})t) \right) \right]. \end{aligned} \quad (42)$$

The first term in Eq. (42) is the noise-free intermediate frequency term (IF), the second term corresponds to noise of the LO laser down-converted by the signal, and the third term corresponds to noise of the signal laser down-converted by the LO. RIN leads to a random fluctuation of the photocurrent amplitude at the intermediate frequency (IF) $\omega_{\text{sig}} - \omega_{\text{LO}}$, which is given by the sum of the variances of the statistically independent noise terms in Eq. (42),

$$\begin{aligned} \langle i_{\text{RIN,tot}}^2 \rangle &= \langle |i_{\text{RIN,sig}}|^2 \rangle + \langle |i_{\text{RIN,LO}}|^2 \rangle \\ &= \frac{1}{2} Z_0^{-1} S^2 \left(\hat{E}_{\text{sig}}^2 (\sigma_{x'',\text{LO}}^2 + \sigma_{y'',\text{LO}}^2) + \hat{E}_{\text{LO}}^2 (\sigma_{x'',\text{sig}}^2 + \sigma_{y'',\text{sig}}^2) \right) \\ &= Z_0^{-1} S^2 \left(\hat{E}_{\text{sig}}^2 \hat{W}_{\sigma,\text{RIN,LO}} + \hat{E}_{\text{LO}}^2 \hat{W}_{\sigma,\text{RIN,sig}} \right) \Delta f \\ &= 2S^2 \left(P_{\text{sig}} \hat{W}_{\sigma,\text{RIN,LO}} + P_{\text{LO}} \hat{W}_{\sigma,\text{RIN,sig}} \right) \Delta f, \end{aligned} \quad (43)$$

for optical powers $P_{\text{sig,LO}} = Z_0^{-1} \langle E_{\text{sig,LO}}^2(t) \rangle = \frac{1}{2} Z_0^{-1} \hat{E}_{\text{sig,LO}}^2$. For given RIN power spectral densities $\hat{w}_{o,\text{RIN}}$, $\hat{w}_{o,\text{RIN,sig}}$ and $\hat{w}_{o,\text{RIN,LO}}$, the current fluctuation due to RIN can now be calculated. However, manufacturers of laser sources do not specify the fluctuation of *optical fields*, but rather the spectrum of the fluctuating *optical power* as measured by recording the spectrum of the fluctuating current with a directly detecting photodiode. The relation between these quantities is derived in Appendix C.

Appendix C: Optical field fluctuation and RIN

The height $\hat{w}_{o,\text{RIN}}$ of the constant optical RIN power spectral density (PSD) for both the signal and the LO source can be calculated from the associated electrical PSD $w_{i,\text{RIN}}(f)$. Many laser manufacturers specify this value in terms of

$$\text{RIN}(f) = \frac{w_{i,\text{RIN}}(f)}{\langle i \rangle^2}. \quad (44)$$

To derive the relation between $\text{RIN}(f)$ and $\hat{w}_{o,\text{RIN}}$, we use a signal representation as in Eq. (16). A harmonic electric field with real amplitude \hat{E} and frequency f_0 is perturbed by complex noise $N(t) = x^m(t) + jy^m(t)$ with a real in-phase noise component $x^m(t)$ and a real quadrature noise component $y^m(t)$,

$$E(t) = [\hat{E} + x^m(t)] \cos(\omega_0 t) - y^m(t) \sin(\omega_0 t) \quad (45)$$

The noise is Gaussian, unbiased such that $\langle x^m(t) \rangle = 0$ and $\langle y^m(t) \rangle = 0$, and the corresponding variances are $\sigma_{x^m}^2 = \sigma_{y^m}^2 = \hat{w}_{o,\text{RIN}} B$ assuming a flat optical PSD within an optical bandwidth B . With the photodetector sensitivity S , the photocurrent becomes

$$i(t) = Z_0^{-1} S \langle E^2(t) \rangle = \frac{1}{2} Z_0^{-1} S (\hat{E}^2 + \langle x^{m2}(t) \rangle + \langle y^{m2}(t) \rangle) \quad (46)$$

Using the Wiener-Khinchine theorem, the (two-sided) PSD $\Theta_i(f)$ can be found by calculating the covariance of the photocurrent, and by applying a Fourier transform,

$$\Theta_i(f) = \int_{-\infty}^{+\infty} \langle i(t) i(t-\tau) \rangle \exp(-j2\pi\tau f) d\tau \quad (47)$$

With Eq. (46), Eq. (47) and when converting the two-sided spectrum $\Theta_i(f)$ to a one-sided spectrum, $w_i(f) = 2\Theta_i(f)$ for $f > 0$, $w_i(f) = 0$ for $f < 0$, the result is

$$w_i(f) = 2S^2 \left(\left(\frac{1}{2} Z_0^{-1} \hat{E}^2 + \hat{w}_{o,\text{RIN}} B \right)^2 \delta(f) + \hat{w}_{o,\text{RIN}} Z_0^{-1} \hat{E}^2 \left[H(f) - H\left(f - \frac{B}{2}\right) \right] + \hat{w}_{o,\text{RIN}}^2 (B-f) [H(f) - H(f-B)] \right) \quad (48)$$

The Heaviside function is defined by $H(f) = 1$ for $f > 0$ and $H(f) = 0$ for $f < 0$. If we exchange $S \rightarrow \alpha$, $\hat{E} \rightarrow P$, and compare the terms in Eq. (48) to [58], Eq. (4, 5-11) and Eq. (4, 5-13), we see that the relations are identical. The first term is disregarded, as an electrical spectrum analyzer measures spectra for frequencies $f > 0$ only such that a spectral DC component $\delta(f)$ is suppressed. The third term stems from photomixing noise with noise and is neglected here because for the given bandwidth $B \approx 1\text{GHz}$ it is a small contribution. The second term $w_{i2}(f) = 2Z_0^{-1} S^2 \hat{w}_{o,\text{RIN}} \hat{E}^2 [H(f) - H(f - B/2)]$ represents the specified electrical RIN(f) for an optical power $P_o = \frac{1}{2} Z_0^{-1} \hat{E}^2$ in terms of the height $\hat{w}_{o,\text{RIN}}$ of the optical PSD,

$$\text{RIN}(f) = \frac{w_{i2}(f)}{\langle i \rangle^2} = \begin{cases} \frac{2Z_0^{-1}S^2\hat{w}_{o,\text{RIN}}\hat{E}^2}{S^2P_o^2} = \frac{4\hat{w}_{o,\text{RIN}}}{P_o} & \text{for } 0 < f < \frac{B}{2}, \\ 0 & \text{else.} \end{cases} \quad (49)$$

For calculating the height $\hat{w}_{o,\text{RIN},\text{sig}}$ and $\hat{w}_{o,\text{RIN},\text{LO}}$ of the optical noise power densities of signal and LO, we need the constant height $\text{RIN}_{\text{spec}} = \text{RIN}(f < B/2)$ of the measured $\text{RIN}(f)$ -spectra together with the optical powers P_{sig} and P_{LO} ,

$$\hat{w}_{o,\text{RIN},\text{sig}} = \frac{1}{4} \text{RIN}_{\text{spec}} P_{\text{sig}}, \quad \hat{w}_{o,\text{RIN},\text{LO}} = \frac{1}{4} \text{RIN}_{\text{spec}} P_{\text{LO}}. \quad (50)$$

Substituting Eq. (50) in Eq. (43) yields (as also obtained in [42]),

$$\langle i_{\text{RIN,tot}}^2 \rangle = S^2 \text{RIN}_{\text{spec}} P_{\text{LO}} P_{\text{sig}} \Delta f. \quad (51)$$

Appendix D: Noise-equivalent power (NEP)

The NEP of a photodetector (unit: $\text{W}/\sqrt{\text{Hz}}$) is defined by the optical signal power P_{NEP} needed to detect the signal within a bandwidth Δf with a power SNR of one, $P_{\text{NEP}} = \text{NEP} \sqrt{\Delta f}$. Considering thermal electronic noise with a current variance $\langle i_{\text{R}}^2 \rangle$ and shot noise $\langle i_{\text{shot}}^2 \rangle = 2eS_{\text{NEP}}P_{\text{NEP}}\Delta f$, where S_{NEP} stands for the photodetector sensitivity at the wavelength where the NEP was measured by the manufacturer, the following relation has to hold:

$$\frac{(S_{\text{NEP}}P_{\text{NEP}})^2}{\langle i_{\text{R}}^2 \rangle + \langle i_{\text{shot}}^2 \rangle} = 1 \quad (52)$$

With the values for our system, $\text{NEP} = 20 \text{ pW}/\sqrt{\text{Hz}}$, $S_{\text{NEP}} = 1 \text{ A/W}$ and $\Delta f = 110 \text{ kHz}$ we calculate $\langle i_{\text{R}}^2 \rangle = 4.4 \times 10^{-17} \text{ A}^2$ and $\langle i_{\text{shot}}^2 \rangle = 2.3 \times 10^{-22} \text{ A}^2$, thus $\langle i_{\text{R}}^2 \rangle \gg \langle i_{\text{shot}}^2 \rangle$. The NEP thus is dominated by electronic noise.

Appendix E: Parameters used for calculation of theoretical curves

The parameters used for the calculations in Section 3.5 and Section 3.6 are summarized in Table 1. The values are derived from data measured during the experiments or in some cases from the specifications provided by the equipment manufacturers.

Table 1. Parameters used for the calculated predictions in Section 3.5 and Section 3.6

Parameter	Values used for calculations
Number of evaluated lines N	7
$P_{m,\text{sig},\lambda_{\text{obj}},\text{meas}}$ for $m = -3\dots3$ for $\kappa = 1$ [dBm]	{-25.6, -17.3, -17.7, -20.2, -20.1, -17.6, -24.5}
$P_{m,\text{LO},\lambda_{\text{obj}},\text{meas}}$ for $m = -3\dots3$ [dBm]	{-23.2, -16.8, -18.2, -20.9, -20.7, -17.8, -22.4}
$P_{m,\text{sig},\lambda_{\text{obj}},\text{ref}}$ for $m = -3\dots3$ [dBm]	{-26.3, -18.0, -18.4, -20.9, -20.8, -18.3, -25.2}
$P_{m,\text{LO},\lambda_{\text{obj}},\text{ref}}$ for $m = -3\dots3$ [dBm]	{-28.9, -22.5, -23.9, -26.6, -26.4, -23.5, -28.1}
$P_{m,\text{sig},\lambda_{\text{cal}},\text{meas}}$ for $m = -3\dots3$ [dBm]	{-30.5, -27.6, -31.1, -31.9, -29.6, -26.6, -33.3}
$P_{m,\text{LO},\lambda_{\text{cal}},\text{meas}}$ for $m = -3\dots3$ [dBm]	{-26.9, -24.8, -28.3, -29.4, -26.9, -23.9, -29.1}
$P_{m,\text{sig},\lambda_{\text{obj}},\text{ref}}$ for $m = -3\dots3$ [dBm]	{-30.6, -27.7, -31.2, -32.0, -29.7, -26.7, -33.4}
$P_{m,\text{LO},\lambda_{\text{obj}},\text{ref}}$ for $m = -3\dots3$ [dBm]	{-39.0, -36.9, -40.4, -41.5, -39.0, -36.0, -41.2}
$RIN_{\text{spec},\lambda_{\text{obj}}}$ [dBc/Hz]	-138
$RIN_{\text{spec},\lambda_{\text{cal}}}$ [dBc/Hz]	-145
$S_{\lambda_{\text{obj}}}$ [A/W]	1.05
$S_{\lambda_{\text{cal}}}$ [A/W]	0.95
R_{TIA} [V/A]	700
Δf [kHz]	110
NEP [$\text{pW}/\sqrt{\text{Hz}}$]	20
Γ_{dB} [dB]	-57
$f_{\text{mod},\text{sig}}$ [GHz]	40

Appendix F: Distribution of optical power between object and calibration measurement

This section is based on the error analysis introduced in Sections 3.3 to 3.5. The signal-to-noise power ratio $\text{SNR}_{m,\lambda}$ of the heterodyne IF line signals is proportional to the powers of the comb lines $P_{m,\text{sig},\lambda}, P_{m,\text{LO},\lambda}$ received by the detectors, see Eq. (15). Signal and calibration combs are generated with the same modulators, which tolerate a limited input power only. This input power limitation restricts the achievable SNR and thus the achievable measurement precision. Therefore the relative optical power distribution between the object and the calibration laser has to be considered as a function of the reflection coefficient κ associated with backscattering of power from the sample surfaces. The power received at 1300 nm from the calibration mirror remains constant, so no dependency on κ is to be expected for the standard deviation $\sigma_{z,\text{cal}}$ of the calibration measurement.

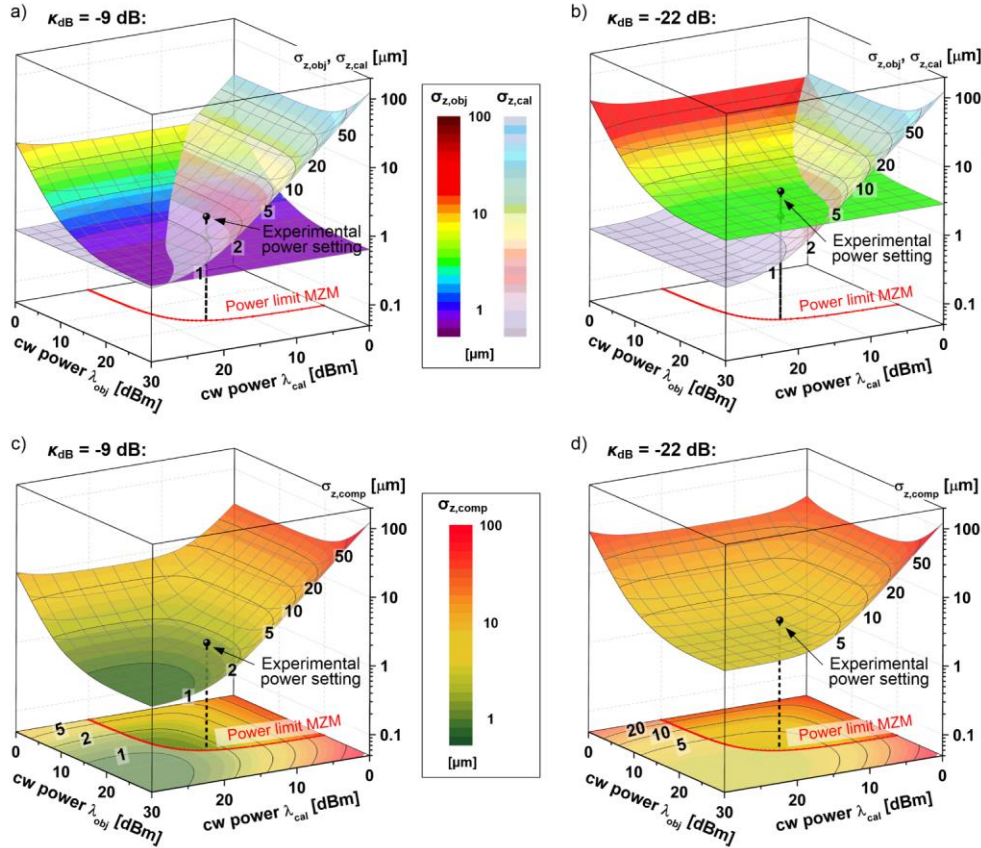


Fig. 13. Calculated standard deviations of the distance measurements as a function of laser input powers into the MZM comb generators for two different values of the object reflection κ_{dB} . Experimental power settings are marked by black dots (calibration laser: 15 dBm, object laser: 18 dBm). The 20 dBm input power limitation of the MZM is indicated by a red line. (a) Individual calculated standard deviations $\sigma_{z,obj}$ and $\sigma_{z,cal}$ for $\kappa_{dB} = -9$ dB. (b) Individual calculated standard deviations $\sigma_{z,obj}$ and $\sigma_{z,cal}$ for $\kappa_{dB} = -22$ dB. (c) Calculated standard deviation $\sigma_{z,comp}$ for $\kappa_{dB} = -9$ dB. (d) Calculated standard deviation $\sigma_{z,comp}$ for $\kappa_{dB} = -22$ dB.

Figure 13 illustrates the system performance for the reflections $\kappa_{dB} = -9$ dB, Fig. 13(a) and 13(c), and $\kappa_{dB} = -22$ dB, Fig. 13(b) and 13(d), and for different laser power levels entering the MZM comb generators. The calculated standard deviations of object and calibration measurements, Fig. 13 (a) and 13(b), as well as of the compensated measurements, Fig. 13 (c) and 13(d), are displayed as surface plots. The limited launch power of maximum 20 dBm into the used MZM poses an additional constraint and is marked by the red line. The standard deviation belonging to the experimental power settings are marked in each subfigure with a black dot. Comparing Fig. 13(a) and 13(b), it can be seen that for $\kappa_{dB} = -9$ dB the standard deviation $\sigma_{z,cal}$ of the calibration measurement dominates, while for smaller object reflections $\kappa_{dB} = -22$ dB the standard deviation $\sigma_{z,obj}$ of the object measurement is larger. This is also illustrated in Fig. 7.

The compensated measurement has a standard deviation which is always larger than either $\sigma_{z,cal}$ or $\sigma_{z,obj}$. In our experiments, standard deviations of 2 μm for $\kappa_{dB} = -9$ dB and 5 μm for $\kappa_{dB} = -22$ dB, can be achieved, Fig. 13(c) and (d). As many technical samples lead to reflection coefficients in that range, the experimental power settings represent a well-chosen trade-off, resulting in standard deviations close to minimum values for the compensated measurement.

Funding

H2020 European Research Council (ERC) (100010663), Starting Grant ‘EnTeraPIC’ (280145); Alfried Krupp von Bohlen und Halbach Foundation; Baden-Wuerttemberg Stiftung gGmbH; Carl Zeiss AG.

Acknowledgments

This work was supported by Carl Zeiss AG, by the Karlsruhe School of Optics & Photonics (KSOP), by the Helmholtz International Research School for Teratronics (HIRST), by the Karlsruhe Nano-Micro Facility (KNMF), and by the ERC Starting Grant EnTeraPIC.

References and links

1. I. Coddington, W. C. Swann, L. Nenadovic, and N. R. Newbury, “Rapid and precise absolute distance measurements at long range,” *Nat. Photonics* **3**(6), 351–356 (2009).
2. M. Cui, M. G. Zeitouny, N. Bhattacharya, S. A. van den Berg, and H. P. Urbach, “Long distance measurement with femtosecond pulses using a dispersive interferometer,” *Opt. Express* **19**(7), 6549–6562 (2011).
3. K. Minoshima and H. Matsumoto, “High-Accuracy Measurement of 240-m Distance in an Optical Tunnel by use of a Compact Femtosecond Laser,” *Appl. Opt.* **39**(30), 5512–5517 (2000).
4. J. Lee, S. Han, K. Lee, E. Bae, S. Kim, S. Lee, S.-W. Kim, and Y.-J. Kim, “Absolute distance measurement by dual-comb interferometry with adjustable synthetic wavelength,” *Meas. Sci. Technol.* **24**(4), 45201–45209 (2013).
5. T.-A. Liu, N. R. Newbury, and I. Coddington, “Sub-micron absolute distance measurements in sub-millisecond times with dual free-running femtosecond Er fiber-lasers,” *Opt. Express* **19**(19), 18501–18509 (2011).
6. S. A. van den Berg, S. T. Persijn, G. J. Kok, M. G. Zeitouny, and N. Bhattacharya, “Many-Wavelength Interferometry with Thousands of Lasers for Absolute Distance Measurement,” *Phys. Rev. Lett.* **108**(18), 183901 (2012).
7. K.-N. Joo and S.-W. Kim, “Absolute distance measurement by dispersive interferometry using a femtosecond pulse laser,” *Opt. Express* **14**(13), 5954–5960 (2006).
8. N. R. Doloca, K. Meiners-Hagen, M. Wedde, F. Pollinger, and A. Abou-Zeid, “Absolute distance measurement system using a femtosecond laser as a modulator,” *Meas. Sci. Technol.* **21**(11), 115302 (2010).
9. M. U. Piracha, D. Nguyen, I. Ozdur, and P. J. Delfyett, “Simultaneous ranging and velocimetry of fast moving targets using oppositely chirped pulses from a mode-locked laser,” *Opt. Express* **19**(12), 11213–11219 (2011).
10. Q. D. Pham and Y. Hayasaki, “Optical frequency comb interference profilometry using compressive sensing,” *Opt. Express* **21**(16), 19003–19011 (2013).
11. S. Yokoyama, T. Yokoyama, Y. Hagiwara, T. Araki, and T. Yasui, “A distance meter using a terahertz intermode beat in an optical frequency comb,” *Opt. Express* **17**(20), 17324–17337 (2009).
12. X. Wang, S. Takahashi, K. Takamasu, and H. Matsumoto, “Spatial positioning measurements up to 150 m using temporal coherence of optical frequency comb,” *Precis. Eng.* **37**(3), 635–639 (2013).
13. J. Lee, Y.-J. Kim, K. Lee, S. Lee, and S.-W. Kim, “Time-of-flight measurement with femtosecond light pulses,” *Nat. Photonics* **4**(10), 716–720 (2010).
14. K. Minoshima, T. Tomita, H. Nakayama, Y. Yamaoka, and H. Matsumoto, “Ultrahigh-resolution distance meter using a frequency comb of a femtosecond mode-locked laser,” in *The Thirteenth International Conference on Ultrafast Phenomena* (OSA, 2002), pp. TuB3.
15. V. Ataie, P. P. Kuo, A. Wiberg, Z. Tong, C. Huynh, N. Alic, and S. Radic, “Ultrafast Absolute Ranging by Coherent Parametric Comb,” in *Optical Fiber Communication Conference* (Optical Society of America, 2013), OTh3D2.
16. H. Zhang, X. Wu, H. Wei, and Y. Li, “Compact Dual-Comb Absolute Distance Ranging With an Electric Reference,” *IEEE Photonics J.* **7**(3), 1–8 (2015).
17. P. Trocha, M. Karpov, D. Ganin, M. H. P. Pfeiffer, A. Kordts, S. Wolf, J. Krockenberger, P. Marin-Palomo, C. Weimann, S. Randel, W. Freude, T. J. Kippenberg, and C. Koos, “Ultrafast optical ranging using microresonator soliton frequency combs,” *Science* **359**(6378), 887–891 (2018).
18. M.-G. Suh and K. J. Vahala, “Soliton microcomb range measurement,” *Science* **359**(6378), 884–887 (2018).
19. Y. Salvadé, N. Schuhler, S. Lévêque, and S. Le Floch, “High-accuracy absolute distance measurement using frequency comb referenced multiwavelength source,” *Appl. Opt.* **47**(14), 2715–2720 (2008).
20. S. Hyun, M. Choi, B. J. Chun, S. Kim, S.-W. Kim, and Y.-J. Kim, “Frequency-comb-referenced multi-wavelength profilometry for largely stepped surfaces,” *Opt. Express* **21**(8), 9780–9791 (2013).
21. C. Weimann, M. Fratz, H. Wölfelschneider, W. Freude, H. Höfler, and C. Koos, “Synthetic-wavelength interferometry improved with frequency calibration and unambiguity range extension,” *Appl. Opt.* **54**(20), 6334–6343 (2015).
22. X. Wu, H. Wei, H. Zhang, L. Ren, Y. Li, and J. Zhang, “Absolute distance measurement using frequency-sweeping heterodyne interferometer calibrated by an optical frequency comb,” *Appl. Opt.* **52**(10), 2042–2048 (2013).

23. E. Baumann, F. R. Giorgetta, J.-D. Deschênes, W. C. Swann, I. Coddington, and N. R. Newbury, "Comb-calibrated laser ranging for three-dimensional surface profiling with micrometer-level precision at a distance," *Opt. Express* **22**(21), 24914–24928 (2014).
24. L. C. Sinclair, I. Coddington, W. C. Swann, G. B. Rieker, A. Hati, K. Iwakuni, and N. R. Newbury, "Operation of an optically coherent frequency comb outside the metrology lab," *Opt. Express* **22**(6), 6996–7006 (2014).
25. H. Wu, T. Zhao, Z. Wang, K. Zhang, B. Xue, J. Li, M. He, and X. Qu, "Long distance measurement up to 1.2 km by electro-optic dual-comb interferometry," *Appl. Phys. Lett.* **111**(25), 251901 (2017).
26. H. Hofler, C. Baulig, A. Blug, M. Dambacher, N. Dimopoulos, H. Wolfelschneider, W. Osten, C. Gorecki, and E. L. Novak, "SPIE Proceedings," pp. 296–306.
27. M.-C. Amann, T. Bosch, M. Lescure, R. Myllylä, and M. Rioux, "Laser ranging: a critical review of usual techniques for distance measurement," *Opt. Eng.* **40**(1), 10–19 (2001).
28. T. Sakamoto, T. Kawanishi, and M. Izutsu, "Asymptotic formalism for ultraflat optical frequency comb generation using a Mach-Zehnder modulator," *Opt. Lett.* **32**(11), 1515–1517 (2007).
29. T. Sakamoto, T. Kawanishi, and M. Izutsu, "Widely wavelength-tunable ultra-flat frequency comb generation using conventional dual-drive Mach-Zehnder modulator," *Electron. Lett.* **43**(19), 1039–1040 (2007).
30. R. Noe, H. Rodler, A. Ebber, G. Gaukel, B. Noll, J. Wittmann, and F. Auracher, "Comparison of polarization handling methods in coherent optical systems," *J. Lightwave Technol.* **9**(10), 1353–1366 (1991).
31. C. Weimann, D. Meier, S. Wolf, Y. Schleitzer, M. Totzeck, A. Heinrich, F. Hoeller, J. Leuthold, W. Freude, and C. Koos, "Fast high-precision distance measurements on scattering technical surfaces using frequency combs," in *Conference on Lasers and Electro-Optics 2013*, CTu2I3.
32. C. E. Towers, D. P. Towers, D. T. Reid, W. N. MacPherson, R. R. J. Maier, and J. D. C. Jones, "Fiber interferometer for simultaneous multiwavelength phase measurement with a broadband femtosecond laser," *Opt. Lett.* **29**(23), 2722–2724 (2004).
33. S. Chang, C.-C. Hsu, T.-H. Huang, W.-C. Chuang, Y.-S. Tsai, J.-Y. Shieh, C.-Y. Leung, and others, "Heterodyne interferometric measurement of the thermo-optic coefficient of single mode fiber," *Zhongguo Wuli Xuekan* **38**, 437–442 (2000).
34. R. E. Bartolo, A. B. Tveten, and A. Dandridge, "Thermal Phase Noise Measurements in Optical Fiber Interferometers," *IEEE J. Quantum Electron.* **48**(5), 720–727 (2012).
35. A. K. Melikov, U. Krüger, G. Zhou, T. L. Madsen, and G. Langkilde, "Air temperature fluctuations in rooms," *Build. Environ.* **32**(2), 101–114 (1997).
36. Corning, *SMF-28e+ Optical Fiber Product Information*, 2014.
37. C. E. Lee, J. J. Alcoz, Y. Yeh, W. N. Gibler, R. A. Atkins, and H. F. Taylor, "Optical fiber Fabry-Perot sensors for smart structures," *Smart Mater. Struct.* **1**(2), 123–127 (1992).
38. P.-E. Dupouy, M. Büchner, P. Paquier, G. Tréneç, and J. Vigué, "Interferometric measurement of the temperature dependence of an index of refraction: application to fused silica," *Appl. Opt.* **49**(4), 678–682 (2010).
39. D. B. Leviton and B. J. Frey, "Temperature-dependent absolute refractive index measurements of synthetic fused silica," *ArXiv e-prints*, 0805.0091 (2008).
40. P. de Groot and S. Kishner, "Synthetic wavelength stabilization for two-color laser-diode interferometry," *Appl. Opt.* **30**(28), 4026–4033 (1991).
41. C. Koos, C. Weimann, and J. Leuthold, Multiscale distance measurement with frequency combs, US9976843B2.
42. S. Yun, G. Tearney, J. de Boer, N. Iftimia, and B. Bouma, "High-speed optical frequency-domain imaging," *Opt. Express* **11**(22), 2953–2963 (2003).
43. J. Ronnau, S. Haimov, and S. P. Gogineni, "The effect of signal-to-noise ratio on phase measurements with polarimetric radars," *Remote Sens. Rev.* **9**(1-2), 27–37 (1994).
44. T. G. McRae, M. T. L. Hsu, C. H. Freund, D. A. Shaddock, J. Herrmann, and M. B. Gray, "Linearization and minimization of cyclic error with heterodyne laser interferometry," *Opt. Lett.* **37**(13), 2448–2450 (2012).
45. L. S. Schuetz, J. H. Cole, J. Jarzynski, N. Lagakos, and J. A. Bucaro, "Dynamic thermal response of single-mode optical fiber for interferometric sensors," *Appl. Opt.* **22**(3), 478–483 (1983).
46. P. R. Bevington and D. K. Robinson, *Data reduction and error analysis for the physical sciences*, 3rd ed. (McGraw-Hill, ©2003).
47. U. Vry, "Absolute Statistical Error in Two-wavelength Rough-surface Interferometry (ROSI)," *Opt. Acta (Lond.)* **33**(10), 1221–1225 (1986).
48. P. Pavliček and J. Soubusta, "Theoretical measurement uncertainty of white-light interferometry on rough surfaces," *Appl. Opt.* **42**(10), 1809–1813 (2003).
49. C. Weimann, P. C. Schindler, R. Palmer, S. Wolf, D. Bekele, D. Korn, J. Pfeifle, S. Koeber, R. Schmogrow, L. Alloatti, D. Elder, H. Yu, W. Bogaerts, L. R. Dalton, W. Freude, J. Leuthold, and C. Koos, "Silicon-organic hybrid (SOH) frequency comb sources for terabit/s data transmission," *Opt. Express* **22**(3), 3629–3637 (2014).
50. M. Lauermann, C. Weimann, A. Knopf, W. Heni, R. Palmer, S. Koeber, D. L. Elder, W. Bogaerts, J. Leuthold, L. R. Dalton, C. Rembe, W. Freude, and C. Koos, "Integrated optical frequency shifter in silicon-organic hybrid (SOH) technology," *Opt. Express* **24**(11), 11694–11707 (2016).
51. C. Weimann, M. Lauermann, F. Hoeller, W. Freude, and C. Koos, "Silicon photonic integrated circuit for fast and precise dual-comb distance metrology," *Opt. Express* **25**(24), 30091–30104 (2017).
52. Carl Zeiss Industrielle Messtechnik GmbH, *O-INSPECT. Multisensor-Messgeräte*, 2013.
53. *KMG angewendet für Längenmessungen. (ISO 10360-2:2009)* (Beuth, 2010).

54. N. Senin, R. Groppetti, L. Garofano, P. Fratini, and M. Pierni, "Three-Dimensional Surface Topography Acquisition and Analysis for Firearm Identification," *J. Forensic Sci.* **51**(2), 282–295 (2006).
55. U. Sakarya, U. M. Leloğlu, and E. Tunalı, "Three-dimensional surface reconstruction for cartridge cases using photometric stereo," *Forensic Sci. Int.* **175**(2-3), 209–217 (2008).
56. Z. J. Geradts, J. Bijhold, R. Hermsen, and F. Murtagh, "Image matching algorithms for breech face marks and firing pins in a database of spent cartridge cases of firearms," *Forensic Sci. Int.* **119**(1), 97–106 (2001).
57. N. R. Newbury, I. Coddington, and W. Swann, "Sensitivity of coherent dual-comb spectroscopy," *Opt. Express* **18**(8), 7929–7945 (2010).
58. S. O. Rice, "Mathematical Analysis of Random Noise," *Bell Syst. Tech. J.* **23**(3), 282–332 (1944).